

Extracellular spikes and CSD

Klas H. Pettersen¹, Henrik Lindén¹, Anders M. Dale², and Gaute T. Einevoll^{1,3}

¹Department of Mathematical Sciences and Technology, Norwegian University of Life Sciences, 1432 Ås, Norway

²Departments of Radiology and Neurosciences, University of California, San Diego, 9500 Gilman Drive, La Jolla, CA 92093-0662, USA

³Center for Integrative Genetics (CIGENE), Norwegian University of Life Sciences, 1432 Ås, Norway

*Chapter to appear in
Handbook of Neural Activity Measurement,
edited by Romain Brette and Alain Destexhe*

April 2011

Contents

1	Extracellular spikes and CSD	1
1.1	Introduction	1
1.2	Biophysical origin of extracellular potentials	3
1.2.1	Biophysical forward-modeling formula	3
1.2.2	Numerical forward-modeling scheme	6
1.2.3	Current-source density (CSD)	7
1.3	Local-field potential (LFP) from single neuron	8
1.3.1	Characteristic features of LFP	8
1.3.2	Low-pass filtering of LFP	11
1.4	Extracellular signatures of action potentials	16
1.4.1	Example forward-modeling result	16
1.4.2	Dendritic sticks and AC length constant	19
1.4.3	Low-pass filtering for the ball-and-stick neuron	21
1.4.4	Parameter dependence of spike amplitude	23
1.4.5	Active dendritic conductances	25
1.5	Extracellular potentials from columnar population activity . .	26
1.5.1	Columnar population model	26
1.5.2	Population response	28
1.5.3	Spatial spread of LFP and MUA signals	28
1.5.4	MUA as a measure of population firing rate	30
1.6	Estimation of current-source density (CSD) from LFP	31
1.6.1	Standard CSD method	31
1.6.2	Inverse CSD methods	33
1.6.3	Validation of iCSD with population forward modeling	35
1.7	Concluding remarks	38

Chapter 1

Extracellular spikes and CSD

1.1 Introduction

Extracellular recordings have been, and still are, the main workhorse when measuring neural activity *in vivo*. In single-unit recordings sharp electrodes are positioned close to a neuronal soma, and the firing rate of this particular neuron is measured by counting *spikes*, that is, the standardized extracellular signatures of action potentials [31]. For such recordings the interpretation of the measurements is straightforward, but complications arise when more than one neuron contribute to the recorded extracellular potential. For example, if two firing neurons of the same type have about the same distance from their somas to the tip of the recording electrode, it may be very difficult to sort the spikes according to from which neuron they originate.

The use of two (*stereotrode* [50]), four (*tetrode* [24, 33, 77, 90]) or more [9] close-neighbored recording sites allows for improved spike sorting, since the different distances from the electrode tips or contacts allow for triangulation. With present recording techniques and clustering methods one can sort out spike trains from tens of neurons from single tetrodes and hundreds of neurons with multishank electrodes [9].

Information about spiking is typically extracted from the high frequency band ($\gtrsim 500$ Hz) of extracellular potentials. Since these high-frequency signals generally stem from an unknown number of spiking neurons in the immediate vicinity of the electrode contact, it is called *multi-unit activity (MUA)*. The low-frequency part ($\lesssim 500$ Hz) of extracellular potentials is called the *local field potential (LFP)*. In *in vivo* recordings the LFP is typically due to dendritic processing of synaptic inputs, not firing of action potentials [14, 44, 54, 68]. The interpretation of LFP is difficult as it is a less local measure of neural activity than MUA; the LFP measured at any point will typically have sizable contributions from neurons located several hundred micrometers away [5, 35, 37, 42–44, 46, 68, 91]. The analysis of LFP data has thus generally been restricted to the estimation of *current source den-*

sity (CSD), the volume density of net transmembrane currents through the neuronal membranes [54, 61, 66], based on linear (laminar) multi-electrode recordings [13, 14, 58, 76, 87]. While CSD analysis cannot separate out contributions from different spatially intermingled neuronal populations (unlike the newly developed *laminar population analysis (LPA)* [14]), the CSD is still easier to interpret than the less localized LFP signal. New silicon-based multicontact probes in various other geometrical arrangements, such as 'multi-shank' [9] or 'needlepad' [64], are rapidly being developed, and the *inverse current-source density (iCSD)* method has been introduced to estimate CSDs in such situations [38, 39, 66].

The estimation of CSD from measured LFP is a so called 'inverse problem' which cannot be solved without imposing additional constraints on the form of the CSD [38, 39, 61, 66]. However, the corresponding 'forward problem', i.e., calculation of the LFP from a known CSD distribution, is well-posed [14, 38, 61, 66]. Likewise, the extracellular potential generated by neurons, both the LFP and the MUA, can be calculated if one knows the transmembrane currents through, and spatial positions of, all parts of the neuronal membranes, and also the extracellular conductivity in the surrounding medium [14, 22, 30, 44, 67, 68].

In the 1960s Rall used such a neuronal forward-modeling scheme to calculate extracellular potentials related to action-potential firing and synaptic interaction using simplified equivalent-cylinder geometries [74, 75]. Thirty years later Holt and Koch combined this scheme with compartmental modeling based on morphologically reconstructed pyramidal neurons, to calculate the extracellular signature of an action potential [30]. This modeling scheme has later been used to calculate other extracellular spike signatures of single neurons [21, 22, 52, 67], MUA from populations of firing neurons [68], and LFP from synaptically activated neurons and neuronal populations [14, 44, 68]. A convenient feature of the forward-modeling scheme is that due to the linearity of Maxwell's equations, the contributions to the extracellular potential from the various neuronal sources add up linearly, and the calculation of extracellular potentials from joint activity in populations with thousands of morphologically reconstructed neurons may even be done on desktop computers [68].

In the next section we describe the biophysical origin of the extracellular potentials and the mathematical formalism connecting it to the underlying neural activity. In Section 1.3 we illustrate the biophysical forward-modeling scheme by investigating the LFP generated by a single pyramidal neuron activated by apical synapses. This example also illustrates some general salient features of LFP, in particular an unavoidable low-pass filtering effect due to the dendritic distribution of transmembrane return currents [44] (also in the absence of inherent frequency-dampening in the extracellular medium [2, 47]). In Section 1.4 we describe results from a forward-modelling study of the influence of the dendritic morphology on the size and shape of the

extracellular spike [67], and in Section 1.5 we correspondingly investigate the LFP and MUA generated by a synaptically activated model population of about 1000 morphologically reconstructed pyramidal neurons, mimicking the sensory-evoked response in a population of layer-5 neurons in rat whisker (barrel) cortex [68]. In Section 1.6 we discuss the problem of CSD estimation, and in particular outline the principles behind the iCSD method [38, 39, 66]. Some concluding remarks are given in the final section.

1.2 Biophysical origin of extracellular potentials

From an electrical point of view cortical tissue consists of a tightly packed collection of neurons and other cells embedded in a low-resistance extracellular medium filling less than a fifth of the total volume [65]. The low resistance of the extracellular medium implies that neighboring cells typically are electrically decoupled and that the difference between the extracellular potential recorded at different positions will be small, typically less than a millivolt. In contrast, the potential difference across the highly resistant cell membranes, that is, the membrane potential, is typically between 50 and 100 millivolts.

1.2.1 Biophysical forward-modeling formula

The extracellular potentials are generated by transmembrane currents, and in the commonly used *volume conductor theory* the system can be envisioned as a three-dimensional smooth extracellular continuum with the transmembrane currents represented as *volume current sources* [65]. In this theoretical framework the fundamental relationship describing the extracellular potential $\phi(t)$ at position \mathbf{r} due to a transmembrane current $I_0(t)$ at position \mathbf{r}_0 is given by [26, 65]

$$\phi(\mathbf{r}, t) = \frac{1}{4\pi\sigma} \frac{I_0(t)}{|\mathbf{r} - \mathbf{r}_0|} . \quad (1.1)$$

Here the extracellular potential ϕ is set to be zero infinitely far away from the transmembrane current, and σ is the *extracellular conductivity*, assumed to be *real, scalar* (the same in all directions) and *homogeneous* (the same at all positions).

The validity of Eq. (1.1) relies on several assumptions:

- A. *Quasistatic approximation of Maxwell's equations:* This amounts to neglecting the terms with the time derivatives of the electric field \mathbf{E} and the magnetic field \mathbf{B} from the original Maxwell's equation, i.e.,

$$\nabla \times \mathbf{E} = -\frac{\partial \mathbf{B}}{\partial t} \approx 0 , \quad (1.2)$$

$$\nabla \times \mathbf{B} = \mu_0 \mathbf{j} + \mu_0 \epsilon_0 \frac{\partial \mathbf{E}}{\partial t} \approx \mu_0 \mathbf{j} , \quad (1.3)$$

so that the electric (Eq. 1.2) and magnetic (Eq. 1.3) field equations effectively decouple [26]. With $\nabla \times \mathbf{E} = 0$ it follows that the electric field \mathbf{E} in the extracellular medium is related to an extracellular potential ϕ via

$$\mathbf{E} = -\nabla\phi . \quad (1.4)$$

For the frequencies inherent in neural activity, i.e., less than a few thousand hertz, the quasistatic approximation seems to be well justified (see, e.g., argument on p. 426 of [26]).

- B. *Linear extracellular medium:* Linear relationship between the current density \mathbf{j} and the electrical field \mathbf{E} ,

$$\mathbf{j} = \sigma\mathbf{E} . \quad (1.5)$$

This constitutive relation is quite general, and σ in Eq. (1.5) may in principle be (i) a *tensor*, accounting for different conductivities in different directions [61], (ii) *complex*, accounting also for capacitive effects [65], and/or (iii) *position-dependent*, that is, vary with spatial position. (Note that Eq. (1.5) is valid only in the frequency domain. In the time domain \mathbf{j} is generally given as a temporal convolution of σ and \mathbf{E} [4]. However, in the case of a frequency independent σ , cf. point E below, Eq. (1.5) will also be valid in the time domain.)

- C. *Ohmic (resistive) medium:* Imaginary part of the conductivity σ is assumed to be zero, that is, the capacitive effects of the neural tissue is assumed to be negligible compared to resistive effects. This appears to be well fulfilled for the relevant frequencies in extracellular recordings [47, 65].
- D. *Isotropic (scalar) extracellular conductivity:* Conductivity σ is assumed to be the same in all directions, i.e., $\sigma_x = \sigma_y = \sigma_z = \sigma$. Measurements from visual cortex in monkeys indeed found the conductivities to be comparable across different directions in cortical grey matter; in white matter, however, the conductivity was found to be anisotropic [47]. However, recent measurements from somatosensory barrel cortex in rats found the conductivity in the vertical direction to be up to 50% larger than in the horizontal directions [23]. Early measurements on frog and toad cerebella also revealed anisotropy in the conductivity [61].
- E. *Frequency-independent extracellular conductivity:* Conductivity σ is assumed to be the same for all relevant frequencies, i.e., $\sigma(\omega)$ is constant. The validity of this assumption is still debated: while some studies have measured negligible frequency dependence [47, 61], other investigations have suggested otherwise [1–3, 20]; cf. chapter by Bedard and Destexhe in present volume.

F. *Homogeneous extracellular conductivity:* Extracellular medium is assumed to have the same conductivity everywhere. This appears to be roughly fulfilled within cortical gray matter [23, 47] and frog and toad cerebella [61], but maybe not in the hippocampus [48]. Further, white matter has a lower conductivity than cortical grey matter which in turn has a lower conductivity than the cell-free cerebral spinal fluid (CSF) [65].

While Eq. (1.1) requires all assumptions A-F to be fulfilled, the expression can be generalized to apply also for other situations. For example:

- If assumption E is violated and σ varies with frequency, Eq. (1.1) can still be used separately for each Fourier component $\hat{I}_0(\omega)$ of the transmembrane current $I_0(t)$ with $\sigma(\omega)$ inserted in the denominator of the equation. Since the extracellular potential ϕ is linear in the transmembrane current I_0 , a simple Fourier sum over the contributions from all Fourier components will provide the total extracellular potential [67]; see also chapter by Bedard and Destexhe in present volume.
- For the case where the conductivity is anisotropic, i.e., assumption D is violated, the equations still apply if the denominator $4\pi\sigma|\mathbf{r} - \mathbf{r}_0|$ is replaced by $4\pi\sqrt{\sigma_y\sigma_z(x - x_0)^2 + \sigma_z\sigma_x(y - y_0)^2 + \sigma_x\sigma_y(z - z_0)^2}$ [61].
- In situations with piecewise constant conductivities, for example with discontinuities in σ at the interfaces between grey and white matter or between the grey matter and the cortical surface, assumption F is violated. However, a generalized version of Eq. (1.1) can be derived based on the 'method of images' [14, 22, 62, 66].

Eq. (1.1) applies to the situation with a single transmembrane current I_0 , but since contributions from several transmembrane current sources add linearly, the equation straightforwardly generalizes to a situation with many transmembrane current sources. With N current point sources the formula in Eq. (1.1) generalizes to

$$\phi(\mathbf{r}, t) = \frac{1}{4\pi\sigma} \sum_{n=1}^N \frac{I_n(t)}{|\mathbf{r} - \mathbf{r}_n|}. \quad (1.6)$$

In Fig. 1.1 we illustrate this formula for the situation where all transmembrane currents come from a single compartmentalized 'ball-and-stick' neuron; it is clear that the measured extracellular potential will not only depend on the position of the electrode, but also the distribution of transmembrane currents.

Fig. 1.1 further illustrates an important 'conservation' law when calculating extracellular potentials due to neural activity: Kirchhoff's current law

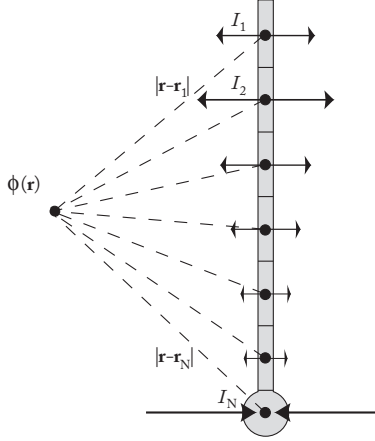


Figure 1.1: Illustration of mathematical formula Eq. (1.6) providing the extracellular potential from transmembrane currents in a single neuron. The size and direction of the arrows illustrate the amplitudes and directions of the transmembrane currents.

implies that the net transmembrane current (including the capacitive current) coming out of a neuron at all times must equal zero. Thus with the neuron depicted in Fig. 1.1 divided into N compartments, one must at all times have $\sum_{n=1}^N I_n(t) = 0$. Therefore a one-compartment model cannot generate any extracellular potential since the net transmembrane current necessarily will be zero. The simplest model producing an extracellular potential is a two-compartment model where transmembrane current entering the neuron at one compartment leaves at the other compartment. The simplest possible multipole configuration is thus the current *dipole*.

1.2.2 Numerical forward-modeling scheme

The numerical evaluation of extracellular potentials naturally splits into two stages [30, 44, 67, 68]:

1. Calculation of transmembrane currents for all neuronal membrane segments using multicompartment neuron models [80], typically using neural simulation tools such as NEURON [10] or Genesis [7].
2. Calculation of the extracellular potential on the basis of the modeled transmembrane currents and their spatial position using a forward-modeling formula similar to Eq. (1.6).

When a neuron is split into N compartments, the formula in Eq. (1.6) should be used with \mathbf{r}_n corresponding to a characteristic 'mean' position for compartment n , e.g., the center of a spherical soma compartment or the mid-point of a cylindrical dendritic compartment. This scheme corresponds to

the so called *point-source* approximation [30, 67] since all transmembrane currents into the extracellular medium from a particular compartment are assumed to go through a single point. Another scheme, the *line-source* approximation, assumes the transmembrane currents from each cylindrical compartment to be evenly distributed along a line corresponding to the cylinder axis [30, 67]. A line-source formula, analogous to the point-source formula in Eq. (1.6), can be found in Ref. [67] (Eq. 2). Unless otherwise noted all forward-modeling calculations with morphologically reconstructed neurons presented in this chapter use the line-source approximation. Further, a frequency-independent, scalar and homogeneous extracellular conductivity with a numerical value of $\sigma = 0.3 \text{ S/m}$ [26] is assumed.

1.2.3 Current-source density (CSD)

The forward-modeling formula in Eq. (1.6) can be mathematically reformulated as

$$\phi(\mathbf{r}, t) = \frac{1}{4\pi\sigma} \iiint_V \frac{C(\mathbf{r}', t)}{|\mathbf{r} - \mathbf{r}'|} d^3 r' . \quad (1.7)$$

when we introduce the quantity $C(\mathbf{r}, t) \equiv \sum_{n=1}^N I_n(t) \delta^3(\mathbf{r} - \mathbf{r}_n)$. Here $\delta^3(\mathbf{r})$ is the three-dimensional Dirac δ -function, and the volume integral goes over all transmembrane currents. The quantity $C(\mathbf{r}, t)$ is called the *current source density (CSD)*, has dimension A/m^3 , and is in general interpreted as the volume density of current entering or leaving the extracellular medium at position \mathbf{r} [54, 61, 65]. A negative $C(\mathbf{r}, t)$ corresponds to current leaving the extracellular medium and is thus conventionally called a *sink*. Likewise, current entering the extracellular medium is called a *source*. The CSD is easier to relate to the underlying neural activity than the extracellular potential itself, and current-source density analysis has thus become a standard tool for analysis of the low-frequency part (LFP) of such potentials recorded with linear (laminar) multielectrodes [61, 66].

While Eq. (1.7) gives the numerical recipe for calculating the extracellular potential given the CSD, a formula providing the opposite relationship can also be derived. Following Refs. [61, 62, 65] we have for the situation with an ohmic extracellular medium that current conservation requires

$$\nabla \cdot \mathbf{j}_{tot} = \nabla \cdot (\sigma \mathbf{E} + \mathbf{j}_s) = 0 , \quad (1.8)$$

where \mathbf{j}_s is the so called *impressed* transmembrane currents entering the extracellular medium [62, 65]. With the additional use of Eq. (1.4) one obtains

$$\nabla \cdot (\sigma(\mathbf{r}) \nabla \phi(\mathbf{r}, t)) = -C(\mathbf{r}, t) , \quad (1.9)$$

where $C(\mathbf{r}, t) \equiv -\nabla \cdot \mathbf{j}_s(\mathbf{r}, t)$. This equation is not only valid for the case with position-dependent σ , but also when it depends on direction, i.e., is a

tensor [61]. In the special case where σ is isotropic and homogeneous, the equation simplifies to

$$\sigma \nabla^2 \phi(\mathbf{r}, t) = -C(\mathbf{r}, t) . \quad (1.10)$$

This equation, called Poisson's equation, is well known from standard electrostatics where it describes how potentials are generated by electrical charges (with the conductivity σ replaced by the dielectric constant ε) [32]. As emphasized in Ref. [65], however, these two versions of Poisson's equation represent different physical processes.

1.3 Local-field potential (LFP) from single neuron

1.3.1 Characteristic features of LFP

To illustrate the forward-modeling scheme and highlight some salient features of LFP we here calculate the extracellular potential around a reconstructed layer-5 model pyramidal neuron from cat visual cortex [49] receiving a single excitatory synaptic input in the apical dendrite. For simplicity the neuron is considered to have purely passive neuronal membranes and to be excited by a synaptic input current $I_s(t)$ modeled as an α -function, that is,

$$I_s(t) = I_0 t / \tau_s e^{1-t/\tau_s} \theta(t) , \quad (1.11)$$

where $\theta(t)$ is the Heaviside unit step function. A time constant $\tau_s = 1$ ms is chosen, and I_0 is set to give a peak EPSP amplitude in the soma of about 0.5 mV. The model is linear, that is, all calculated extracellular and intracellular potentials are proportional to I_0 , making the model somewhat easier to analyze than when non-linear currents are involved. However, most qualitative features is expected to be unchanged if we, e.g., considered excitation by a set of conductance-based synapses instead.

In Fig. 1.2A we show the calculated extracellular potential traces at a set of positions outside the neuron. An important feature which is immediately apparent is that the shape and amplitude of the extracellular potentials depend on position. Near the apical synaptic input the extracellular signature is always negative, reflecting that the excitatory current-synapse providing a current sink dominates the sum in the forward-model formula, cf. Eq. (1.6). At positions close to the soma the extracellular potential is always positive, reflecting that return currents in the soma area dominate the sum. At other positions, for example above the synapse, a biphasic extracellular potential is observed. Interestingly, there is not a monotonous decay of the amplitude with distance from the synaptic input: large extracellular responses are observed close to the soma, almost a millimeter away.

Another important feature is the observed increased half-width of the extracellular potentials recorded close to the soma compared to those in the vicinity of the synaptic input. This is illustrated by the two insets

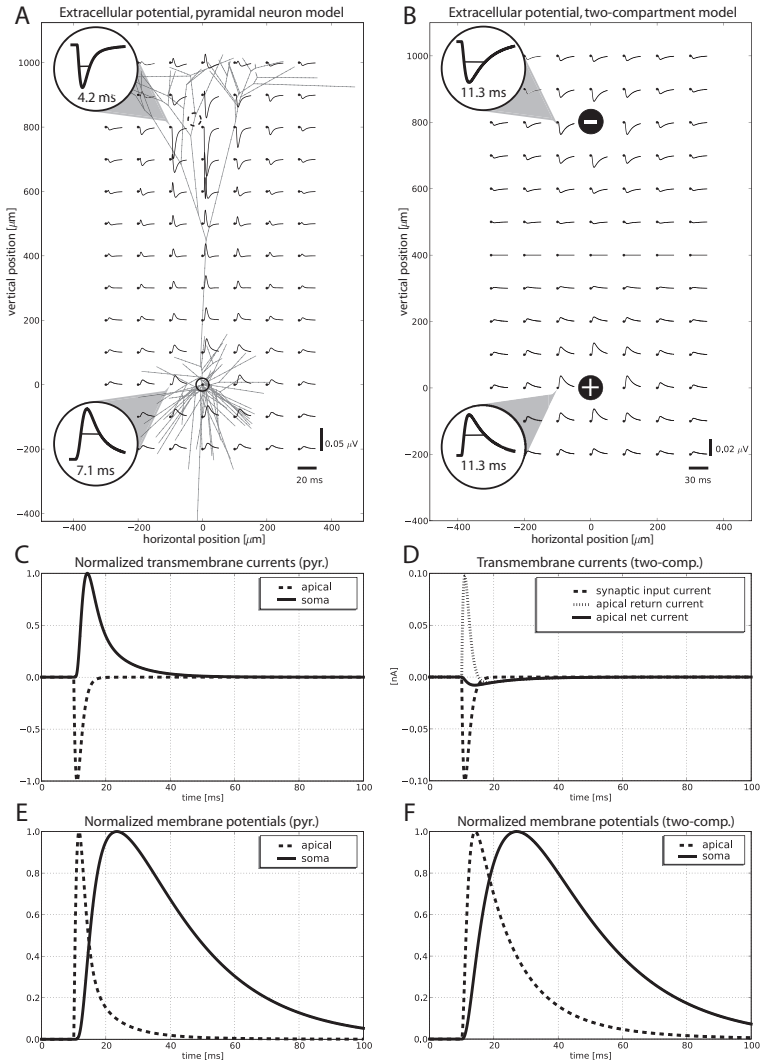


Figure 1.2: Calculated extracellular potentials following an excitatory synaptic input into purely passive neuron models. The synapse is current-based and modeled as an α -function $I_s(t - t_{on})$ (Eq. 1.11) with $\tau_s = 1$ ms, $I_0 = 0.1$ nA and the onset time t_{on} set to 10 ms. (A) Results for reconstructed L5 pyramidal neuron from Ref. [49] with active channels removed. Passive parameters: membrane resistivity $R_m = 30000 \Omega\text{cm}^2$, axial resistivity $R_i = 150 \Omega\text{cm}$, membrane capacitance $C_m = 0.75 \mu\text{F}/\text{cm}^2$. Potentials are shown in a 20 ms window starting 2 ms prior to synaptic onset. Dashed circle denotes position of synapse. (B) Results for analogous two-compartment neuron model. The apical (top) and soma (bottom) compartments have resistive (r_a, r_s) and capacitive (c_a, c_s) membrane elements, are connected to each other via the resistance r_{as} . The same synaptic current as in A is inserted into the apical compartment. Model parameters: $r_a = 318 \text{ M}\Omega$, $r_s = 95 \text{ M}\Omega$, $r_{as} = 358 \text{ M}\Omega$, $c_a = 71 \text{ pF}$, $c_s = 236 \text{ pF}$. The point-source approximation is used, cf. Eq. (1.6). (C) Normalized transmembrane currents at the synaptic input segment and at the soma for the pyramidal neuron in A. Half-widths are 2.5 ms and 6.5 ms, respectively. (D) Synaptic input current, return current, and net transmembrane current for the apical compartment in two-compartment model. Half-widths are 2.5 ms, 2.3 ms and 5.2 ms, respectively. (E) Normalized membrane potential for synaptic input segment and soma segment for the pyramidal neuron model. Half-widths are 4.1 ms and 33 ms, respectively. (F) Normalized membrane potential of apical and soma compartments of two-compartment model. Half-widths are 13 ms and 38 ms, respectively. Extracellular potentials in insets in A and B are scaled arbitrarily.

showing magnified extracellular potential traces in Fig. 1.2A. In the upper inset close to the synapse the width is 4.2 ms, while the width at the lower inset close to soma is 7.1 ms, both widths measured at 50% of the trace's peak amplitudes. Thus the extracellular potential close to the synaptic input contains higher frequencies than the extracellular potential far away from the synaptic current generator.

This feature can be understood on the basis of passive cable properties of the neuron. The transmembrane currents dominating the extracellular potentials close to the soma have been low-pass filtered and have a wider temporal profile compared to the transmembrane currents close to the synaptic input. This is illustrated in Fig. 1.2C where the transmembrane current profile is seen to have a much larger half-width at the soma (~ 6.5 ms) compared to at the dendritic segment containing the synapse (~ 2.5 ms).

An analogous low-pass filtering is seen from the temporal shapes of the apical and somatic membrane potentials, respectively, in Fig. 1.2E. Here the apical EPSP peaks already a couple of milliseconds after synaptic onset and has a half-width of about 4 ms. In contrast the somatic EPSP peaks about 15 ms after synaptic onset and has a half-width of more than 30 ms. The low-pass filtering effect is thus stronger for the membrane potential than for the transmembrane current, and thus also compared to the extracellular potentials.

In Fig. 1.2B we further show calculated extracellular potential traces for an analogous two-compartment model, the simplest neuron model that produces an extracellular potential. The spatial extension corresponds to the distance between the single synapse and the soma for the reconstructed neuron in Fig. 1.2A. This model has only five parameters, the resistances (r_a, r_s) and capacitances (c_a, c_s) of the apical and soma compartments, respectively, and the intercompartment resistance (r_{as}).

The pattern of extracellular responses in the two-compartment model is seen to resemble the pattern for the reconstructed pyramidal neuron in that large negative responses are observed close to the apical compartment while large positive responses are observed close to the soma compartment. However, in the two-compartment model the net transmembrane current in the soma compartment is forced by Kirchhoff's current law to be identical in size, but with opposite sign, compared to the apical compartment. What goes in at one compartment, must leave at the other. Since only these two compartments contribute to the sum in the forward-modeling formula for the extracellular potential (that is, $N = 2$ in Eq. 1.6), the temporal form of the extracellular potential will be the same everywhere; only the sign and size of an overall amplitude will vary. This is illustrated by the two insets showing magnified extracellular traces in Fig. 1.2B which both have half-widths of 11.3 ms. There is thus no *position-dependent* filtering of frequency components in the two-compartment model. At least three neuron compartments are needed to capture such an effect.

There is, however, low-pass filtering also inherent in the two-compartment model as illustrated by the larger half-width of the extracellular potential (11.3 ms) observed in Fig. 1.2B compared to the half-width of the synaptic input current (2.5 ms) in Fig. 1.2D. This reflects that in a two-compartmental model like this, where both compartments have a resistive and a capacitive component, the axial current going between the compartments is not equal to the imposed synaptic current in the apical compartment. Instead it is the difference between the synaptic current and the return current of the apical compartment. This axial current corresponds in magnitude to the net transmembrane currents at the two compartments, and as illustrated in Fig. 1.2D these net transmembrane currents are both smaller in amplitude and temporally wider than the synaptic current. In Fig. 1.2F we in fact observe an even larger low-pass filtering effect for the membrane potential compared to results for the reconstructed model neuron in Fig. 1.2E.

In Lindén et al. [44] we discuss in detail how the LFP patterns depend on neuronal morphologies, spatial positions of the driving synapse, as well as electrode recording positions.

1.3.2 Low-pass filtering of LFP

The frequency content of LFP and EEG signals has attracted significant interest in particular since power laws, i.e., power spectra scaling as $1/f^\beta$, have commonly been observed [2, 4, 8, 18, 28, 45, 51, 53, 56, 71]. Suggested explanations of these observed power laws have invoked a variety of neural network mechanisms [19, 40, 51, 53], as well as frequency filtering inherent in the extracellular medium [2, 4, 19]. The results above, elaborated in [44], point to an additional source of frequency filtering of the LFP and EEG: extended dendritic morphologies will due to their passive cable properties unavoidably give a separate frequency-filtering effect for the extracellular potentials. In fact there are two dendrite-based filtering mechanisms: (i) a higher fraction of the apical synaptic input current will propagate to the soma for low frequencies than high frequencies, and (ii) extracellular potentials recorded far away from the synaptic input current will have more low frequencies than those recorded close to the input current due to the low-pass filtering of the return current by the dendritic tree. The simple two-compartment model only displayed the first type of filtering, while the reconstructed pyramidal neuron model displayed both types.

A comprehensive investigation of these filtering effects is beyond the scope of this chapter; for this we refer to Lindén et al. [44]. However, some example results illustrating the important principles are shown in Fig. 1.3. The same pyramidal neuron as in Fig. 1.2A is considered, now with sinusoidal currents $I_s(t) = I_0 \cos(2\pi ft)$ inserted at ten apical synapses. The extracellular potential is simulated along an axis oriented perpendicular to the primary apical dendrite at the level of the soma.

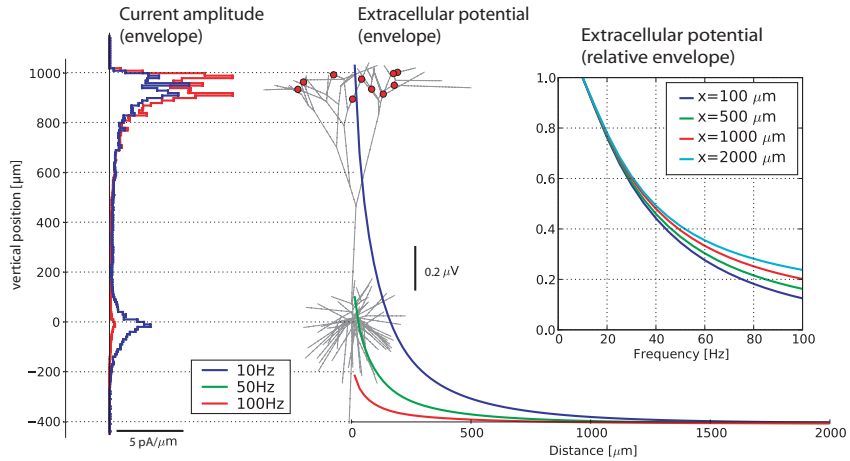


Figure 1.3: Illustration of frequency-filtering of LFP for the passive layer-5 pyramidal model neuron in Fig. 1.2A receiving simultaneous sinusoidal input currents $I_s(t) = I_0 \cos(2\pi ft)$ at 10 apical synapses (red dots in middle panel). The middle panel shows the envelope (amplitude) of the sinusoidally varying extracellular potential plotted at different lateral positions at the level of the soma (x -direction). The left panel shows the envelope of the linear current-source density of the *return current* along the depth direction (z -direction) for $f=10$ Hz and $f=100$ Hz. The right panel shows the relative magnitude of envelopes of the extracellular potential as a function of frequency for different lateral distances from the soma. Here curves are normalized to unity for the lowest frequency considered, $f=10$ Hz.

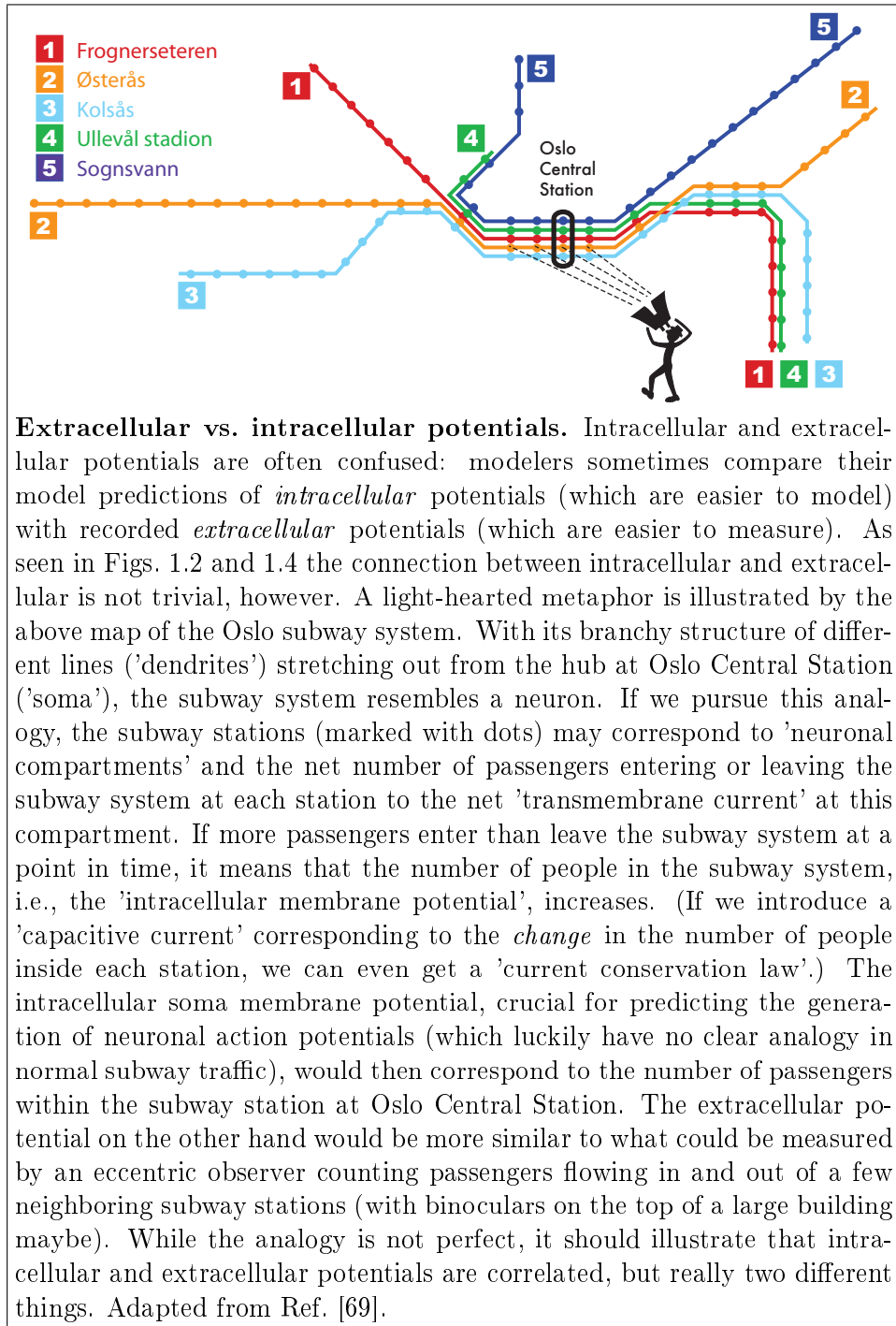
The amplitude of the extracellular potential is plotted in the main (middle) panel. The most obvious feature is the amplitude differences in the extracellular potential for the different frequencies: the amplitude is much larger for the lowest frequency ($f = 10$ Hz) than for the highest frequency ($f = 100$ Hz), even with the same input current amplitude I_0 .

The somatic transmembrane current is usually the most important source for the extracellular potential for proximal recordings at the level of soma. As the frequency increases, the current profile of the return currents tend to become more localized around the synaptic inputs, i.e., a larger fraction of the current returns through the dendrites near the synapses. This is clearly seen in the current profile to the left in Fig. 1.3. The 100 Hz sinusoid has a much larger current apically, and a much smaller current basally, than the 10 Hz sinusoid.

In the right part of Fig. 1.3 we illustrate how the low-pass filtering effect of the extracellular potential depends on the distance from soma. Here all curves are normalized to unity for the lowest frequency considered, $f=10$ Hz. When the frequency is increased, more of the current return apically, further away from any recording position at the depth level of the soma. This implies that the extracellular potential becomes smaller, since the difference in distances between the contributions to the potential from the synaptic input current and the return current will be smaller. Since the distance between the synaptic current generator and the return currents is relatively larger for recordings near the soma than for recordings further away in the lateral direction, the frequency decay of the extracellular potential will be steeper near the soma (small x) than for the distal recordings (large x).

The decay in extracellular amplitude as a function of frequency is not only seen in recordings at the level of the soma, but is also prominent for recordings at the level of the synaptic input (results not shown). The reason is the same: the potential is the sum of the transmembrane currents weighted inversely with distance to the sources, and when the typical distance between the synaptic current generator and the return currents gets smaller, the extracellular potential will also become smaller.

The low-pass filtering effect described here is a general feature always present for spatially extended neuronal-membrane structures [44], and in the next section we will show its impact on the extracellularly recorded signature from an action potential.



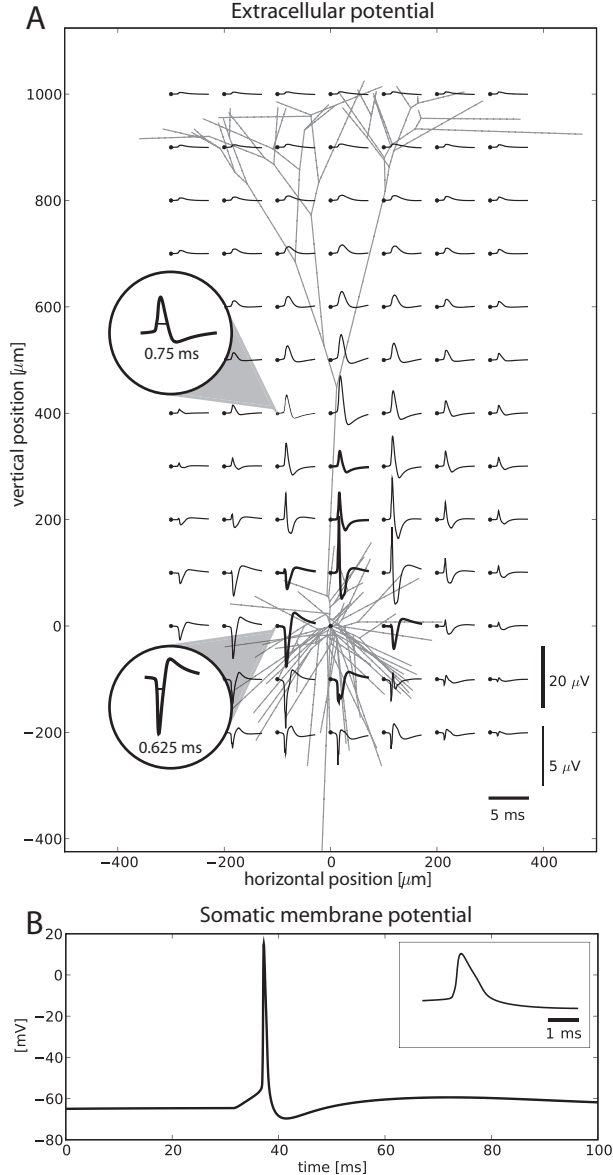


Figure 1.4: (A) Calculated extracellular signature of an action potential in layer-5 pyramidal model neuron taken from Ref. [49]. Neuron is stimulated with apical excitation and basal inhibition similar to 'stimulus input pattern 1' (SIP1) in Ref. [68]. Traces show extracellular potential in 5 ms window around time of spiking. Thick lines corresponds to 20 μ V scaling, thin lines to 5 μ V scaling. Extracellular potentials in the two insets are scaled arbitrarily. (B) Somatic membrane potential during simulation. Inset shows soma potential for same 5 ms time window as for the extracellular potentials in A.

1.4 Extracellular signatures of action potentials

1.4.1 Example forward-modeling result

In a typical single- or multielectrode recording spikes from tens of neurons may be intermingled [9]. When developing automated algorithms for detecting and sorting these spikes according to their true neural source [15, 16, 27, 36, 41, 70, 72, 73, 78, 81, 83, 86, 89], several issues arise: For example, which types of neurons are most likely to be seen in the recordings, which neuronal parameters are important for the spike amplitude and shape, and which parameters determine the decay of the spike amplitude with increasing distance from the neuron? These are important questions also for the interpretation of multi-unit activity (MUA), the high-frequency content of the extracellular potential [14, 67, 68, 79, 87], and for the question of why the firing of neurons in the brain appear to be so sparse [82].

An example forward-modeling result for the extracellular potential related to an action potential is shown in Fig. 1.4A. Again the layer-5 pyramidal model neuron of Ref. [49] is used, this time including active conductances. A combined pattern of apical excitation and basal inhibition is used to excite the action potential, similar to what is labeled 'stimulus input pattern 1' (SIP1) in Ref. [68]. The largest extracellular responses are seen closest to the soma (thick lines in Fig. 1.4A). As the shortest distance considered is as large as $100 \mu\text{m}$, the spike amplitudes depicted in the figure are nevertheless all smaller than $20 \mu\text{V}$ (see Fig. 3 in [68] for a close-up picture of spike shapes closer to the soma). The lowest inset in the figure, showing a magnified extracellular potential, illustrates the typical shape of recorded extracellular spikes: a sharp, deep dip (sodium phase) followed by a shallower, but longer-lasting, positive bump (potassium phase).

As for the spatial LFP patterns in Fig. 1.2, the extracellular spike is also seen to have an inverted sign apically compared to basally. Further, a position-dependent low-pass filtering effect is also observed: the magnified extracellular potential in the top inset in Fig. 1.4A is seen to be wider than at the lower inset closer to the soma. With the extracellular spike-width defined as the width of the sodium phase at 25% of its maximum, a widening from 0.625 to 0.75 ms is observed. This implies that the higher frequencies attenuate faster than the lower frequencies when moving away from the soma. A spike-width increase with increasing distance from the soma has been seen experimentally, and explanations for this in terms of extracellular-medium effects has been suggested [1, 3]. However, it is still debated whether such effects are present in cortical tissue: while some investigators have measured low-pass filtering effects in the extracellular medium [20], other investigators found no such effect [47, 61].

Below we outline how the neuron *morphology*, combined with its *cable properties*, can provide an alternative, or supplementary, explanation

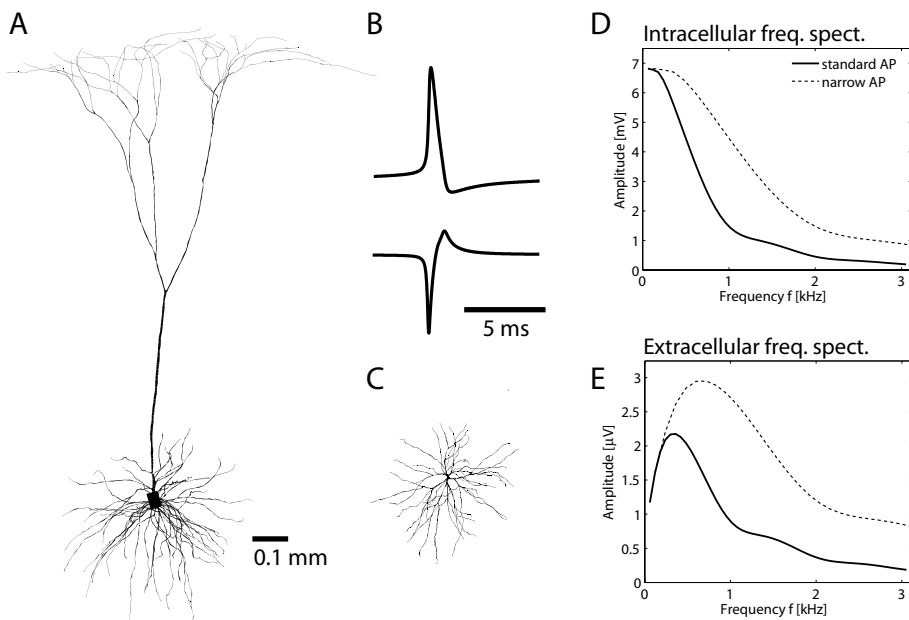


Figure 1.5: (A) Pyramidal layer-5 neuron used in investigation of extracellular spikes [67]. (B) Upper: 'Standard' action potential (AP) used in model study, half-amplitude spike width is 0.55 ms. Lower: Typical shape of corresponding extracellular spike near soma for 'standard' AP. Extracellular spike width is 0.44 ms (see text for definition). (C) Stellate layer-4 neuron used in investigation [67]. (D) Frequency spectrum of intracellular voltage for 'standard' AP in B, and a corresponding 'narrow' AP with identical form but exactly half the spike width. (E) Frequency spectrum of extracellular voltage traces of 'standard' spike in B (solid), and corresponding extracellular voltage trace for 'narrow' spike (dashed). Reconstructed neuron morphologies taken from Ref. [49]. See Ref. [67] for further information.

for the distance-dependent low-pass filtering effect of extracellular spikes [67]. Section 1.2 explained why a neuron model has to contain at least two compartments to produce an extracellular potential at all, and in Section 1.3 it was shown that a two-compartment model could not produce any *distance-dependent* low-pass filtering effect. In Ref. [67] we investigated the effect of the neuronal morphology and the passive dendritic parameters on the extracellular spike signature in detail, in particular the distance dependence of the spike amplitude and low-pass filtering. A variety of neuronal morphologies was considered, both morphologically reconstructed pyramidal (Fig. 1.5A) and stellate cells (Fig. 1.5C) and simplified models built up of dendritic sticks ('ball-and-stick', 'ball-and-star', 'ball-and-bush', cf. Fig. 1 in Ref. [67]). While the shape of the intracellular action potential vary from neuron to neuron, we wanted to focus on how the dendritic structure affects the relationship between the intracellular and extracellular potentials [29, 89]. We thus imposed a standardized intracellular action potential (cf. Fig. 1.5B) in the somas of the neurons in the numerical evaluation of the extracellular spike signatures. In accordance with the qualitative observation in Fig. 1.4A all neuron models were found to exhibit a distance-dependent low-pass filtering effect, that is, larger spike widths further away from soma, cf. Figs. 6 and 7 in Ref. [67]. However, the amplitudes of the spikes were found to be quite different, both their size and their dependence on distance from soma. For example, with identical intracellular action potentials, the spike-amplitude 60 μm away from soma was found to be about 40 mV for the pyramidal neuron, but only about 10 mV for the stellate neuron.

To obtain a better understanding of the phenomenon we also developed a conceptually simpler and more intuitive theory accounting for the observed variation in spike shape and amplitude [67]. This theory also produced analytical predictions of the dependence of the spike amplitude on the dendritic parameters, predictions that later were confirmed by numerical calculations. The essential idea behind the theory is that during an action potential, the soma can be viewed as a voltage source driving current into the soma-attached dendrites, and that the size and shape of the extracellular signature will qualitatively depend on (i) the magnitudes of the axial currents entering the dendrites from the soma, (ii) what distances from the soma the imposed axial currents on average returns through the dendritic membranes and (iii) the number and geometrical arrangement of dendrites. In fact it was found that many of the salient features of the extracellular spike could be understood by considering the simple ball-and-stick neuron model where the soma is modeled as a single compartment and the dendrite as a simple cable stick [34, 67]. With the soma considered as a voltage source, the various soma-attached dendrites are effectively decoupled from each other. Consequently the total extracellular potential generated by a more complex neuron can be approximated as a superposition of contributions from a collection of soma-attached dendritic sticks pointing in different

directions [67].

1.4.2 Dendritic sticks and AC length constant

A concept we found essential to get both an intuitive and quantitative handle on the crucial spatial distribution of the return current along the dendritic stick, is the so called *alternating current (AC) length constant* [67]

Imagine a ball-and-stick neuron model (cf. Fig. 1.6) where the dendritic stick is infinitely long. This *infinite* ball-and-stick neuron is assumed to receive a constant (DC) somatic transmembrane current. Since the membrane currents at all times have to sum to zero, the same amount of current has to return to the extracellular medium through the dendritic stick. The density function of the dendritic return current has the functional form of an exponential decay with the *length constant* (or *space constant*) λ describing the steepness of the decay [12, 67]. More precisely, the length constant is the dendritic position where the steady-state transmembrane return current has decreased to $1/e$ of its value at the soma end, or equivalently, λ is the position where the dendritic return current has its center of gravity. The center of gravity is then defined as the mean of the normalized transmembrane current density weighted by dendritic position.

The length constant is not only useful for describing the neuron's intrinsic qualities (for example electrotonic compactness), it is also useful for understanding the extracellular potentials generated by the neuron. For example, when computing the extracellular potential far away from the neuron (far-field limit), the ball-and-stick neuron model can be approximated by a dipole model [67]. The parameters of the dipole model will then be the dipole current, which equals the somatic current, and the dipole size, which essentially is given by the dendritic length constant, cf. Fig. 1.7A. For infinite dendritic sticks under the DC condition this length constant is given by $\lambda = \sqrt{dR_m/4R_i}$, where d is the stick diameter, R_m is membrane resistivity [Ωcm^2] and R_i is the axial resistivity [Ωcm] [12].

As the length constant is important for understanding several aspects of a neuron (electrotonic compactness, extracellular far-field potential), it is useful to define a general length constant which is not restricted to infinite sticks and DC conditions. In analogy to the definition of the standard DC space constant λ , Ref. [67] define the AC length constant, $\lambda_{\text{AC}}(\omega)$, to be the mean of the absolute value of the current density amplitude weighted with distance, when the dendritic stick is driven by a sinusoidal voltage in the soma-end of the stick. This length constant will be frequency dependent through the angular frequency $\omega = 2\pi f$. For a finite stick this corresponds to (in complex notation)

$$\lambda_{\text{AC}}(\omega) = \frac{\int_0^l z |\hat{\mathbf{i}}_m(z)| dz}{\int_0^l |\hat{\mathbf{i}}_m(z)| dz}, \quad (1.12)$$

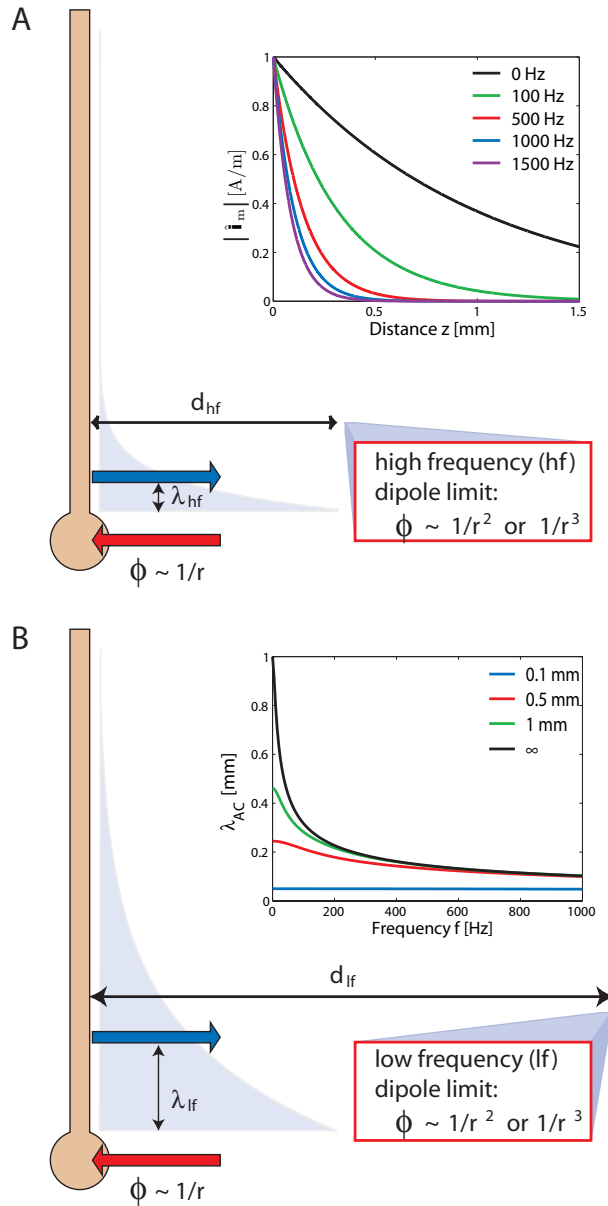


Figure 1.6: Illustration of ball-and-stick neuron and its frequency-dependent dipole sizes and corresponding far-field limits. (A) For high frequencies (hf), the center of gravity (blue arrow) of the dendritic return current is close to soma. Therefore, the AC length constant λ_{hf} is small and transition to the far-field limit occurs around a distance d_{hf} , relatively close to the neuron. Inset: Transmembrane return-current profile along an infinite dendritic stick for different frequencies [67]. Parameter: stick diameter 2 mm, membrane and axial resistivities $R_m = 30000 \Omega\text{cm}^2$, $R_i = 150 \Omega\text{cm}^2$, membrane capacitance $C_m = 1 \mu\text{F}/\text{cm}^2$. $\lambda_{\text{AC}}^\infty$ is 317 mm, 145 mm, 103 mm, and 84 mm for 100 Hz, 500 Hz, 1000 Hz, and 1500 Hz, respectively. (B) For low frequencies (lf) the AC length constant λ_{lf} is relatively large and the far-field limit is reached for a larger distance d_{lf} than for the higher frequency in A. Inset: AC length constant $\lambda_{\text{AC}}(\omega)$ as a function of frequency for ball-and-stick models of different length; parameter values for diameter, resistivity and capacitance are the same as in A.

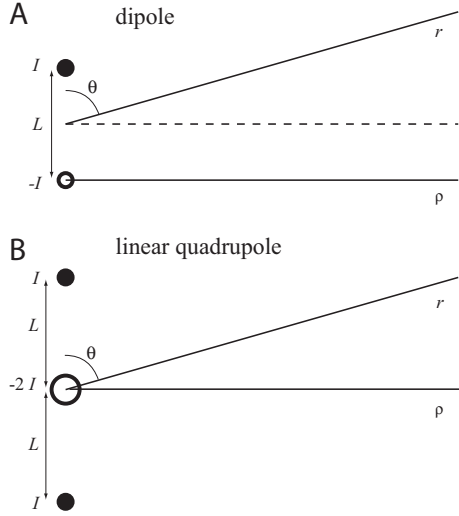


Figure 1.7: Illustration of (A) current dipole and (B) linear current quadrupole.

where the stick is assumed to be extended along the positive z -axis from $z = 0$ (soma end) to $z = l$. $\hat{\mathbf{i}}_m(z)$ denotes the complex transmembrane current density at position z along the stick (where the real part corresponds to the physical transmembrane current). In the inset in Fig. 1.6A we show normalized values for $|\hat{\mathbf{i}}_m(z)|$ as a function of distance from the soma for an infinite ball-and-stick neuron for different frequencies. The higher the frequency, the closer to the soma the return current is seen to be. This is reflected in the frequency-dependence of the AC length constant $\lambda_{AC}(\omega)$ as seen in the inset of Fig. 1.6B: the highest frequencies have the shortest AC length constants. This latter panel also shows that shorter dendritic sticks have shorter $\lambda_{AC}(\omega)$, as expected since the closed ends will force the return currents out closer to the soma. This effect will be most pronounced for the lower frequencies.

For an infinite stick an analytical formula can be found for the AC length constant. In this special case Eq. 1.12 reduces to [34, 67]

$$\lambda_{AC}^\infty(\omega) = \lambda \sqrt{2/[1 + \sqrt{1 + (\omega\tau)^2}]} , \quad (1.13)$$

where τ denotes the membrane time constant, $\tau = R_m C_m$.

1.4.3 Low-pass filtering for the ball-and-stick neuron

In Ref. [67] numerical investigations of the extracellular signature of action potentials in ball-and-stick neurons also revealed a characteristic spike-width increase when moving away from soma, similar to what is seen for the pyramidal neuron in Fig. 1.4A. Here we will outline how a reduced model, a dipole model with a soma compartment attached to a conflated dendritic stick, can

explain the phenomenon. In Section 1.3 we showed that a two-compartment neuron model, i.e., a dipole model with a *fixed* dipole length, cannot express such position-dependent low-pass filtering. The crucial element introduced here is that the dipole model must have a *frequency-dependent dipole length* based on λ_{AC} .

Far way (i.e., far-field limit) from a current dipole with current strength I and length L the extracellular potential is given by [32, 67]

$$\phi_{\text{far,d}}(r, \theta) = \frac{1}{4\pi\sigma} \frac{IL}{r^2} \cos\theta , \quad (1.14)$$

when polar coordinates are used, cf. Fig. 1.7A. This model shows a $1/r^2$ decay when moving in any direction where θ is fixed. However, when moving perpendicular to the dipole (e.g., along the ρ -axis in Fig. 1.7A) the extracellular potential decays as a quadrupole, i.e., as $1/r^3$ [67].

The distance dependence is more complicated for proximal extracellular potentials than for far-field potentials. Close to the soma compartment, the soma current will dominate the potentials, and in this region the distance dependence will be given by the monopole expression

$$\phi_m(r, \theta) = \frac{1}{4\pi\sigma} \frac{I}{r} , \quad (1.15)$$

that is, the amplitude decays as $1/r$. This dipole neuron model therefore predicts a transition in the power of the distance dependence of the extracellular potential from -1 close to the soma to -2 (or -3) in the far-field limit.

If the soma membrane potential oscillates at an angular frequency ω , current will flow from the extracellular medium through the soma and up into the dendritic stick with the same frequency with an amplitude we denote $I(\omega)$. A simple model for the generated extracellular potential around the ball-and-stick neuron can now be made: Near the soma the amplitude of oscillating extracellular potential can be described by Eq. (1.15) with I replaced by $I(\omega)$, and in the far-field limit the extracellular potential amplitude can be described by Eq. (1.14) with I replaced by $I(\omega)$ and L with $\lambda_{\text{AC}}(\omega)$ from Eq. (1.12) [67]. From the dendrite's point of view the soma action potential can be seen as a voltage source enforcing the characteristic intracellular voltage waveform. Since the dendritic stick itself has linear response properties, this waveform can be Fourier decomposed, and each frequency can be treated separately. The extracellular signature of the action potential can thus be found by a simple linear superposition [67].

The extracellular signature at a particular position will depend crucially on whether the frequency components are in the 'close-to-soma-regime' (Eq. 1.15), in the 'far-field limit' (Eq. 1.14), or somewhere in between. The following question thus arises: what decides the distance for which the far-field limit is reached? Clearly, the transition to the far-field limit must

depend on the dipole length, that is, $\lambda_{\text{AC}}(\omega)$. Thus the transition to the far-field limit for each component will depend on frequency. Further, since the highest frequencies will have the smallest $\lambda_{\text{AC}}(\omega)$, these components will reach the far-field limit (where the distance-decay is sharper and the signal rapidly diminishes) closer to soma. Fig. 1.6 illustrates this low-pass filtering effect for the dipole-model approximation of the ball-and-stick neuron.

1.4.4 Parameter dependence of spike amplitude

In addition to explaining the position-dependent low-pass filtering of the extracellular spike, the dipole model approximation of the ball-and-stick neuron can also explain essential features of the size and distance dependence of the spike-amplitude [67]: For the infinite ball-and-stick neuron it is possible to derive an analytical expression for the frequency-dependent *transfer function* \mathbf{T} describing how a soma membrane potential 'transfers' to an extracellular potential. With a complex notation (boldface) the soma membrane potential for a given angular frequency ω can be represented as $\mathbf{V}_0(t; \omega) = \hat{\mathbf{V}}_0(\omega)e^{j\omega t}$, where $\hat{\mathbf{V}}_0$ contains both the amplitude and phase of the sinusoidal potential and $j = \sqrt{-1}$. The physical soma membrane potential will then be the real part of this complex quantity, $V_0(t; \omega) = \text{Re}\{\mathbf{V}_0(t; \omega)\}$. The complex Fourier amplitude of the extracellular potential $\hat{\Phi}(\mathbf{r}, \omega)$ for a ball-and-stick model can thus be related to the complex soma potential $\hat{\mathbf{V}}_0(\omega)$ through the transfer function $\mathbf{T}(\mathbf{r}, \omega)$, i.e., $\hat{\Phi}(\mathbf{r}, \omega) = \mathbf{T}(\mathbf{r}, \omega)\hat{\mathbf{V}}_0(\omega)$ [67]. Since the DC-subtracted intracellular somatic action potential $V_0(t)$ can be expressed by a Fourier series, $V_0(t) = \sum_{k=1}^{\infty} \text{Re}\{\hat{\mathbf{V}}_0(\omega_k)e^{j\omega_k t}\}$, the measured extracellular response to any such DC-subtracted somatic action potential can be expressed as

$$\phi(\rho, z, t) = \sum_{k=1}^{\infty} \text{Re}\{\mathbf{T}(\mathbf{r}, \omega_k)\hat{\mathbf{V}}_0(\omega_k)e^{j\omega_k t}\}. \quad (1.16)$$

The transfer function for the ball-and-stick neuron has a rather complex analytical form [67]. To investigate the parameter dependence of the spike amplitude we instead use the much simpler dipole model with a frequency-dependent dipole length given by the length constant of the infinite ball-and-stick model in Eq. (1.13).

Near the soma the monopole contribution from the soma membrane current will dominate, and the extracellular potential will decay as $|\hat{\Phi}(\omega)| \sim |\hat{\mathbf{I}}(\omega)|/4\pi\sigma r$, where the somatic membrane current \mathbf{I} is related to the somatic membrane potential through the dendrite's admittance, $\hat{\mathbf{I}} = \hat{\mathbf{Y}}\hat{\mathbf{V}}_0$, see [67]. The transfer function \mathbf{T} will therefore be given by $\hat{\mathbf{Y}}/4\pi\sigma r$ in the near-field approximation, and for high frequencies ($\omega\tau \gg 1$), the transfer function can be shown to be [67]

$$|\mathbf{T}_{\text{near}}| \sim \frac{d^{3/2}}{\sigma r} \left(\frac{fC_m}{R_i} \right)^{1/2}. \quad (1.17)$$

In the far-field approximation the potential is given by the dipole or quadrupole expressions (when moving laterally, see above), $\hat{\Phi}(\omega) \sim \hat{\mathbf{I}}(\omega)L/4\pi\sigma r^2$ or $\hat{\Phi}(\omega) \sim \hat{\mathbf{I}}(\omega)L^2/4\pi\sigma r^3$, respectively [67]. We then assume $L \approx \lambda_{AC}^\infty(\omega)$ (Eq. 1.13), and for $\omega\tau \gg 1$ we have $\lambda_{AC}^\infty(\omega) \sim \lambda/\sqrt{\omega\tau} \sim \sqrt{d/fR_iC_m}$. With a reasonable time constant such as $\tau = 20$ ms, this high-frequency approximation holds for frequencies $f \gg 8$ Hz, i.e., all the dominant frequencies of the action potential. The far-field transfer functions can with these assumptions be shown to be [67]

$$|\mathbf{T}_{far,d}| \sim \frac{d^2}{\sigma r^2 R_i}, \quad |\mathbf{T}|_{far,q} \sim \frac{d^{5/2}}{\sigma r^3 f^{1/2} R_i^{3/2} C_m^{1/2}}, \quad (1.18)$$

where 'far,d' means far-field dipole expression and 'far,q' means far-field quadrupole expression (applicable when moving perpendicular to the ball-and-stick neuron [67]). In Pettersen and Einevoll [67] a host of numerical simulations were done to investigate to what extent these analytical predictions are accurate, not only for individual frequency components but also for the full action potential. The numerical calculations indeed confirmed their validity, cf. Fig. 9 in Ref. [67].

The transfer-function expressions in Eqs. (1.17) and (1.18) give some interesting qualitative insights:

1. Close to the soma the higher frequencies are amplified compared to the low frequencies, $|T| \sim \sqrt{f}$. Thus close to the soma the extracellular action potential will typically appear sharper than the intracellular action potential.
2. Far away this high-frequency amplification is either vanished ('far,d', $|T| \sim f^0$) or reversed ('far,q', $|T| \sim 1/\sqrt{f}$).
3. $|T|$ is independent of the membrane resistivity R_m .
4. $|T|$ decreases with increasing intracellular resistivity R_i .
5. $|T|$ may, depending on distance from soma, increase or decrease with increasing capacitance C_m .
6. $|T|$ increases with increasing dendritic diameter d , that is, $T \sim d^k$ where $k = 1.5 - 2.5$.

While Eqs. (1.17) and (1.18) were derived for a simple ball-and-stick, similar expressions can easily be derived for more complicated neuron models, see Ref. [67] for details. For example, for the linear quadrupole model depicted in Fig. 1.7B the quadrupolar far-field expression in Eq. (1.18) applies in all angular directions [67].

The last entry in the above list (point 6) suggests an important connection between the extracellular spike amplitude and the dendritic diameters.

Since the contributions from different soma-attached dendrites add up, the point suggests a rule of thumb: *A neuron's extracellular spike amplitude is approximately proportional to the sum of the dendritic cross-sectional areas of all dendritic branches connected to the soma* [67]. Thus, neurons with many, thick dendrites connected to soma will produce large-amplitude spikes, and will therefore have the largest radius of visibility.

In Ref. [67] we confirmed this rule of thumb for the two morphologically reconstructed cells shown in Fig. 1.5A and C. The pyramidal neuron had more soma-attached dendrites than the stellate cell (11 vs. 6) and they were thicker as well (average diameter of $3.0 \mu\text{m}$ vs. $2.1 \mu\text{m}$). In the numerical simulations the ratio between the peak-to-peak extracellular spike amplitudes of the pyramidal and stellate neurons were found to be 3.3, 3.7, and 4.0 at $20 \mu\text{m}$, $60 \mu\text{m}$, and $100 \mu\text{m}$ distances, respectively (see Table 1 in [67] for details). The above rule of thumb ($|T| \sim d^2$) predicts this ratio to be 4.5, in reasonable agreement with the numerical results. The agreement is even better if one considers that the d^2 -rule is expected to be best far away from the soma. Strictly speaking, a $d^{3/2}$ -rule is predicted close to the soma (Eq. 1.17). The latter rule predicts the ratio to be 3.3, exactly what is calculated for the smallest distance ($20 \mu\text{m}$).

1.4.5 Active dendritic conductances

So far, we have only considered action potentials from neurons with electrically passive dendrites. This assumption makes the problem of translating intracellular potentials in the soma to extracellular potentials recorded outside the neuron *linear* and, importantly, independent of the detailed form of the intracellular action potential, i.e., independent of the detailed properties of the active soma conductances responsible for generating the action potential. Thus the analytical insights reviewed in the previous subsection apply in principle to all different intracellular action-potential waveforms.

However, real neurons have active conductances also in the dendrites [84]. In general, this makes the problem nonlinear, and the trick of considering each frequency component of the action potential separately is no longer applicable. Instead one has to use comprehensive compartmental models including all active conductances explicitly. Gold and coworkers [21, 22] have done thorough investigations of the extracellular signatures of spikes from pyramidal neurons in hippocampus CA1 and fitted compartmental models to reproduce simultaneously recorded intracellular and extracellular waveforms. An important result from their studies was that extracellular waveforms provide tighter constraints on the model parameters than the intracellularly recorded somatic action potentials. This suggested that extracellular action potentials could be a good source of data for constraining compartmental models [21].

Their results are also in qualitative agreement with many of the obser-

vations seen above for the purely passive dendrites: (i) the spike width was seen to increase with distance from the soma (cf. Fig. 5A in Ref. [22]), (ii) the amplitude was seen to decay with soma distance with a power between 1 and 2 for distances less than 50 μm (cf. Fig. 14 in Ref. [22]), and (iii) the amplitude was seen to change significantly to varying intracellular resistivity R_i and capacitance C_m , but not so much to varying membrane resistivity [21].

1.5 Extracellular potentials from columnar population activity

In Sections 1.3 and 1.4 we considered extracellular potentials generated by activity in single neurons. Extracellularly recorded signals like LFP and MUA do not stem from single neurons, however, rather from *populations* of neurons. The forward-modeling scheme applied above for single neurons applies equally well to populations of neurons, and here we outline results from our modeling study of the generated LFP and MUA by a synaptically activated, spatially confined population of layer-5 neurons [68], mimicking a population of large pyramidal cells in a sensory neocortical column [57].

In this pilot MUA and LFP forward-modeling study we sought to answer questions like: Is the MUA really a more local measure of neural activity than LFP? How sharply does the MUA and LFP decay outside the active population? To what extent is the MUA a measure of the *population firing rate*? Do existing CSD analysis methods estimate the true CSD accurately?

1.5.1 Columnar population model

The simulated population in Pettersen et al. [68] consisted of 1040 layer-5 pyramidal neurons of the type shown in Fig. 1.5A. Their somas were placed stochastically in a cylinder with both diameter and height of 0.4 mm, see Fig. 1.8. The population was constructed based on a single neuron model template, but with two different synaptic input patterns. To get MUA responses in reasonable agreement with experimental data [14, 79], only 40 of the neurons received a net synaptic input sufficiently strong to generate a single action potential within a time window of about 20 ms. The net synaptic input to the remaining 1000 neurons was tuned such that no action potential was generated. To introduce temporal jitter in the synaptic activation of the neurons in the population, the neuronal templates were stochastically shifted in the time domain assuming a Gaussian distribution with a standard deviation of 5 ms. The extracellular potential was computed at 23 positions, every 0.1 mm along the center axis of the population, see Fig. 1.8B. For the present modeling example we found that a balanced combination of apical excitation and basal inhibition was needed to get realistic LFP amplitudes

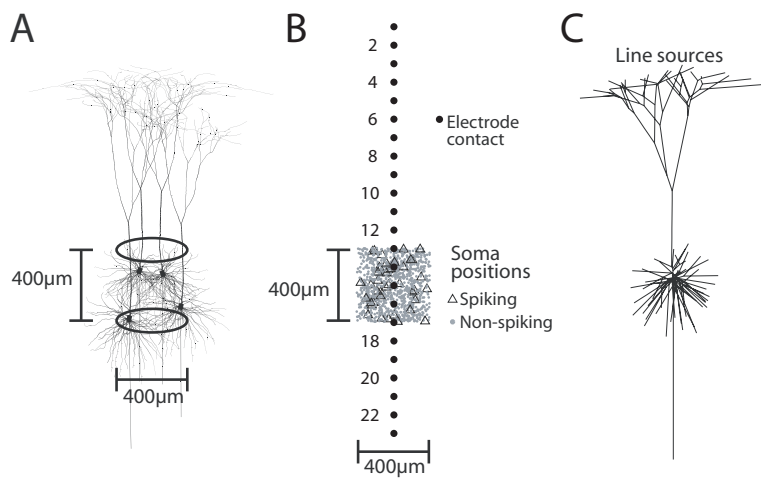


Figure 1.8: (A) Schematic illustration of the population of reconstructed layer-5 pyramidal neurons considered in forward-modeling study [68]. (B) Somas of pyramidal neurons placed randomly inside a cylindrical annulus with height 0.4 mm, outer diameter 0.4 mm and inner diameter 0.1 mm. One thousand neurons were non-spiking (dots), while 40 neurons (triangles) produced a single spike following synaptic stimulation . Extracellular potential was simulated at assumed electrode contact positions along the center axis of the population (filled circles). (C) Illustration of line-source method: the transmembrane current from each neural segment is modelled as a linear current source of uniform current density. Note that each neural branch (section) depicted in the panel may consist of several segments.

compared to experimental LFP data, since apical excitation alone did not give large enough LFP amplitudes for a population of about 1000 cells. Both single-trial and trial-averaged population responses were calculated. A set of 40 trials was considered in the trial-averaging procedure, and each trial differed in their stochastic distribution of both the position and time-shifting for the individual neurons.

1.5.2 Population response

With more than 1000 synaptically activated pyramidal neurons, the LFP response was found to be very robust, different trials gave virtually identical results. For the MUA, the detailed temporal structure of single-trial signals was found to vary considerably on a millisecond scale, reflecting the stochastic firing of specific neurons located close to the electrode contacts (cf. Fig. 4 in [68]). The stochastic placement of the soma positions in the model thus makes single-trial MUA a much more noisy measure of neural activity than LFP. However, the trial-averaged MUA over 40 trials was seen to be quite reproducible and, importantly, independent of the form of synaptic input pattern providing the excitation.

Trial-averaged responses for the LFP and MUA data obtained in our forward modeling scheme are shown in Fig. 1.9A and B. Note that while synaptically evoked LFP can be seen at most electrode contacts, MUA can essentially only be seen at the contacts inside the vertical distribution of somas in the population, i.e., between contacts 13 and 17.

1.5.3 Spatial spread of LFP and MUA signals

If one measures extracellular potentials in cortex with two adjacent electrodes, say, 0.5 millimeter apart and find that their LFP signals are correlated, two possible interpretations come to mind. Either (i) the two electrodes may measure neural activity from two separate neural populations which happen to have correlated synaptic input activity, or (ii) the LFP generated by a single population may spread to the two electrodes by *volume conduction* [65]. Likewise, if the MUA signals of the two electrodes are observed to be correlated, this can also be due to correlated firing in two spatially separated populations or volume conduction of the MUA signal from a single population.

From the discussion in Section 1.4 one would expect the LFP generated by a population to have a larger spatial spread, i.e. larger volume conduction, than the corresponding MUA: the LFP contains lower frequencies than the MUA and will thus have longer characteristic AC length constants and consequently decrease less steeply with distance. These expectations were confirmed by numerical simulations [68]: Fig. 1.9C illustrates the distance-decay of the MUA and LFP signals from our model population in a direction

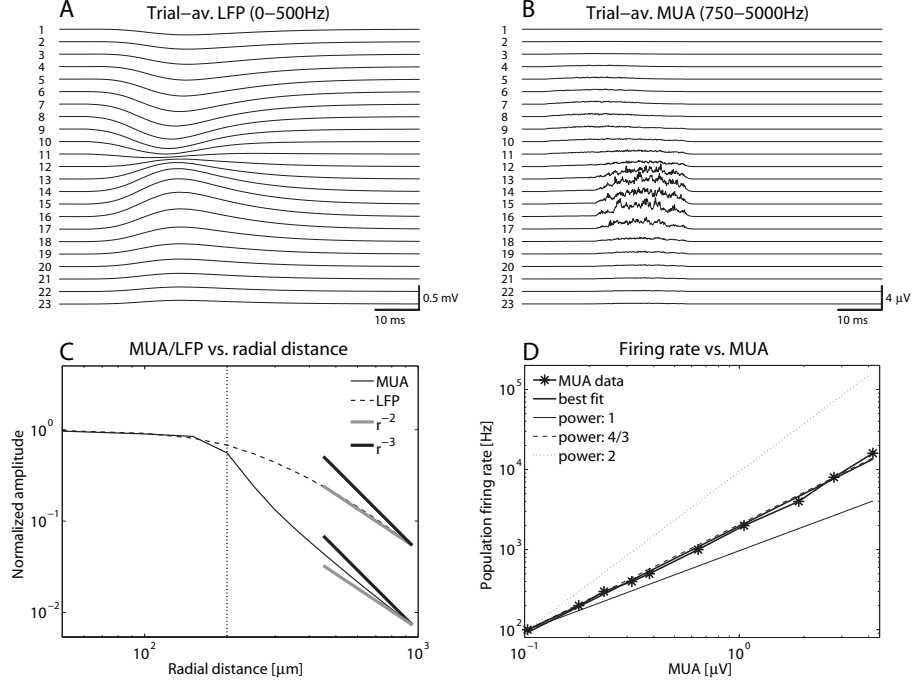


Figure 1.9: Trial-averaged (A) local field potential and (B) multi-unit activity recorded at center axis of cylindrical population of 1040 layer-5 pyramidal neurons receiving apical excitation and basal inhibition. The depicted LFP is obtained by (i) low-pass filtering of the calculated extracellular potential (< 500 Hz) and (ii) trial-averaging ($n=40$). The MUA is obtained by (i) band-pass filtering between 750–5000 Hz, (ii) rectification, and (iii) trial-averaging ($n=40$). 40 of 1040 neurons fire an action potential stochastically within time window of 20 ms. For details of numerical simulation, see Ref. [68]. (C) Decay of amplitude of 'area under graph' MUA and LFP calculated at electrode 15 (middle of population) as a function of lateral distance from the population center, cf. Fig. 15 in [68]. The vertical dotted line illustrates the lateral edge of the soma distribution corresponding to a radial distance of 200 µm. (D) Relationship between 'true' firing rate and estimates based on MUA signal, cf. Fig. 13 in [68]. The depicted MUA is the average MUA for the 5 electrode contacts running through the center of the population (electrode contacts 13–17, see Fig. 1.8). The population size was varied and all neurons within the population were spiking. The power law giving the best fit to the data has a coefficient of 1.346.

perpendicular to its center axis. The MUA is seen to decay sharply outside the population ($r > 200 \mu\text{m}$), whereas the LFP is seen to spread much further. For example, at a position 0.3 mm outside the population cylinder, i.e., 0.5 mm from the population center, the magnitude of the LFP signal is seen to be reduced with about a factor five compared to the value at the population center, whereas the MUA is reduced by a factor 30. Thus compared to the LFP, observed correlations of the MUA signal between adjacently placed electrodes are more likely to be due to correlated firing in two different populations. However, these are just example results, and more systematic studies are needed to elucidate, e.g., the neural origin of LFPs recorded in cortex [42–44].

1.5.4 MUA as a measure of population firing rate

The MUA, obtained by high-pass filtering ($\gtrsim 500 \text{ Hz}$) with subsequent rectification of the extracellular signal, has been assumed to measure the population firing rate for a group of neurons around the electrode contacts [6, 14, 79, 87]. In Ref. [68] we used the present population forward-modeling study to test this assertion: since we can set the population firing rate ourselves in this model world, we have a gold standard against which the calculated MUA signal can be compared.

Two different regimes can be expected [68]: The first regime corresponds to very low firing rates. Here the various extracellular signatures from firing in the nearby neurons contributing to the MUA will not overlap significantly in time. Thus even with biphasic extracellular signatures (cf. Fig. 1.4A), there will be little cancelation between positive and negative phases of the extracellular potential. A linear relationship between the MUA and the population firing rate is thus expected.

The other regime corresponds to very high population firing rates. In this high-firing limit the MUA was found to grow roughly as the square root of the population firing rate [68]. Here there will be strong temporal overlap in the sum over extracellular signatures from all contributing neurons, and the summation is better viewed as a sum over randomly drawn positive and negative contributions to the extracellular potential. If the positive and negative contributions are similar in size, the rectified summed signal is expected to grow as the square root of the number of contributions, i.e., as the square root of the population firing rate.

It is, however, *a priori* unclear what ranges of population firing rates correspond to the different regimes; this will depend on neuronal morphologies and densities (as well as the physical characteristics of the electrode). In Pettersen et al. [68] it was found that for realistic population firing-rates and trial-averages over 40 trials, there is a large regime where the relationship between the MUA and population firing rate is well approximated by raising the population firing rate to a power of $3/4$, i.e., intermediate between the

1.6. ESTIMATION OF CURRENT-SOURCE DENSITY (CSD) FROM LFP31

linear and the square-root regimes. This implied that a good estimate of the population firing rate can be obtained by raising the MUA to the power $4/3$, see double-logarithmic plot in Fig. 1.9D. Indeed, this rule clearly improved the population firing rate estimates for the examples considered in Ref. [68] compared to results from using the standard linear rule. However, it is unclear to what extent this rule extends to other situations.

1.6 Estimation of current-source density (CSD) from LFP

The previous Sections 1.3, 1.4, and 1.5 all considered forward-modeling of extracellular potentials, that is, the calculation of extracellular potentials from known activity in neurons. The present section deals with the opposite problem, namely how the underlying neural activity can be estimated based on measurements of the extracellular potential or more specifically the LFP. An estimation of transmembrane current through a particular segment of a particular neuron is in practice out of the question; in principle, one can only extract one unknown current source per electrode contact and an infinite number of different current-source constellations can produce the extracellular potential recorded on a finite number of electrode contacts.

A common strategy has been to use multicontact LFP recordings to estimate the current-source density (CSD), that is, the volume density of net current entering or leaving the extracellular medium, see Section 1.2.3. A microscopic view inside the cortical tissue reveals an inhomogeneous, densely packed collection of neural segments acting as current sources. The CSD is a more mesoscopic concept and can be interpreted as the average transmembrane current for a piece of neural tissue in a volume element a few tens of micrometers across. In practice the maximum possible spatial resolution in the estimation of CSD will be limited by the intercontact distance, typically 100 μm or more.

1.6.1 Standard CSD method

The traditional CSD estimation is based on LFP recordings with laminar (linear) multielectrode arrays with a constant inter-contact distance h inserted perpendicularly to the cortical surface [13, 14, 54, 76, 79, 87]. Motivated by the prominent laminar structure of cortical tissue where the changes in the lateral directions are much smaller than in the vertical direction, it has been common to assume an infinite activity diameter in the lateral (xy) plane, i.e., perpendicular to the laminar electrode oriented in the z -direction. Variation of the extracellular potential in the x - and y -directions can then

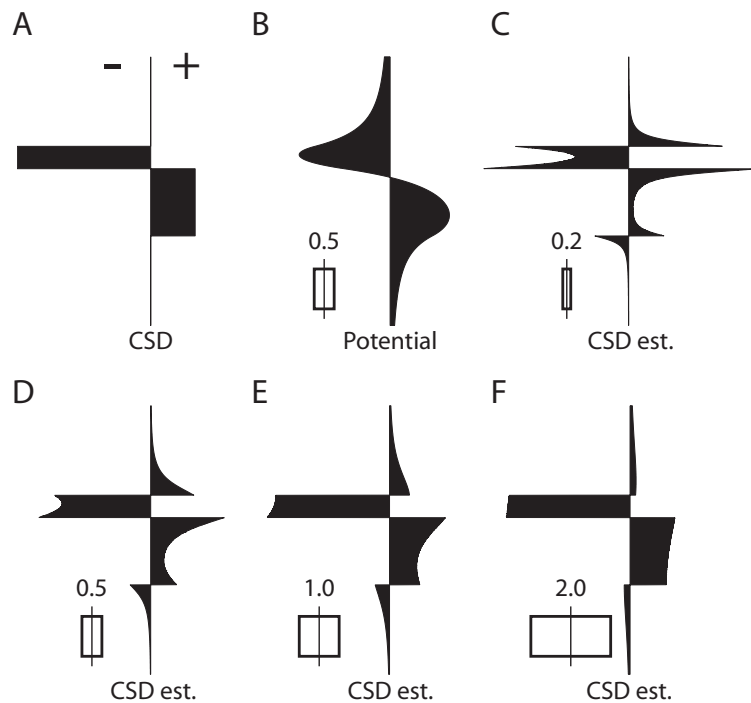


Figure 1.10: Illustration of errors inherent in standard CSD estimation method for one-dimensional recordings for simplified CSD profile, similar to Ref. [61]. (A) Example CSD depth profile, (B) corresponding LFP at center axis when the CSD distribution has a diameter-to-height ratio of 0.5. (C–F) Estimated CSDs for increasing diameter-to-height ratios, as indicated by the number and inset in the lower left of each panel. All estimates are based on the double spatial-derivative formula of the standard CSD method, i.e., Eq. (1.20). Arbitrary units, negative values to the left and positive to the right.

1.6. ESTIMATION OF CURRENT-SOURCE DENSITY (CSD) FROM LFP33

be neglected, so that Eq. (1.10) simplifies to its one-dimensional version:

$$\sigma \frac{d^2\phi(z,t)}{dz^2} = -C(z,t) . \quad (1.19)$$

A natural estimator for the CSD at electrode position z_j has thus been [61]

$$C(z_j) = -\sigma \frac{\phi(z_j + h) - 2\phi(z_j) + \phi(z_j - h)}{h^2} \quad (1.20)$$

or variations thereof, including additional spatial smoothing filters [17, 87]. With N electrode contacts the above estimator can predict the CSD only at the $N - 2$ interior contact positions. However, a trick allowing for the estimation of the CSDs also at the top and bottom electrodes has been suggested [88].

If we define the domain of electrode contact j located at position z_j as the domain from $z_j - h/2$ to $z_j + h/2$, it is natural to assume that the estimate $C(z_j)$ should correspond to the average CSD within this domain. In Ref. [66] it was instead shown from electrostatic theory that the process of discretizing the one-dimensional Poisson equation into Eq. 1.20 corresponds to assuming all CSD within each electrode's domain to be located in an infinitely thin (and infinitely wide) sheet at the height of the electrode-contact. However, a possibly larger source of estimation error stems from the assumption of an infinite activity diameter perpendicular to the laminar electrode. This was noted already by Nicholson and Freeman in 1975 [61] who showed that small 'columnar' activity diameters (~ 1 mm or less) may give large errors in the estimated CSD. The numerical example from Ref. [61] is reproduced here in Fig. 1.10, and for the small source diameters the estimated CSD is clearly seen to be erroneous, predicting, for example, spurious sinks and sources. Indeed Nicholson and Freeman [61] recommended and later pursued a full three dimensional CSD analysis based on the full Poisson equation (Eq. 1.10) which required technically demanding measurements of extracellular potentials in all three spatial directions [63]. With the advent of the present silicon-based multielectrodes such a CSD estimation scheme can now become more practically feasible [9].

1.6.2 Inverse CSD methods

In Pettersen et al. [66] a new method for estimation of CSD was introduced, the *inverse CSD (iCSD)* method. The core idea behind this method is to exploit the well-known forward-modeling scheme for calculation of the LFP from given a CSD distribution: With an assumed form of the CSD distribution parameterized by N unknown parameters, the forward solution can be calculated and inverted to give estimates of these N parameters based on N recorded potentials. This iCSD approach has several inherent advantages:

- The method does not rely on a particular geometrical arrangement of the N electrode contacts recording the LFP signals. It is thus not only applicable to linear multielectrodes [66], but can also be straightforwardly be generalized to other multielectrode geometries [38, 39].
- A priori constraints, such as knowledge about the lateral size of columnar activity, can be built directly into the iCSD estimator [14, 39, 66, 68].
- Unlike the standard CSD method, the iCSD method can also predict CSD at the positions of the boundary electrode contacts [38, 39, 66].
- Discontinuities and direction dependence of the extracellular conductivity can be incorporated [14, 66].

To present the iCSD idea more explicitly we now consider a situation where one has recordings from N electrode contacts. Further, the CSD has been parameterized by N parameters describing the weights of the different contributions to the CSD [66]. Regardless of the choice of parametrization, the CSD is now uniquely determined by the N weight parameters $\{C_1, C_2, \dots, C_N\}$. The LFP due to this CSD distribution can then be calculated at the N electrode contact positions using electrostatic theory (e.g., using Eq. (1.7) if σ is scalar and homogeneous). Due to the linearity of electrostatic theory the LFP grows linearly with the CSD weight parameters, and their relationship can thus be formulated in matrix form as [66]

$$\Phi = \mathbf{F}\mathbf{C} . \quad (1.21)$$

Here $\Phi = [\phi_1 \ \phi_2 \ \dots \ \phi_N]^T$ is a vector containing the extracellular potential, and $\mathbf{C} = [C_1 \ C_2 \ \dots \ C_N]^T$ is a corresponding vector containing the CSD parameters. \mathbf{F} is an $N \times N$ matrix containing the mapping from CSDs to extracellular potentials found from electrostatic theory. If \mathbf{F} is constructed properly, it will be invertible, and an estimate of the N unknown CSD parameters $\hat{\mathbf{C}}$ can then be estimated from the N recorded potentials by a simple matrix multiplication with the inverse matrix \mathbf{F}^{-1} :

$$\hat{\mathbf{C}} = \mathbf{F}^{-1}\Phi \quad (1.22)$$

To illustrate the calculation of the matrix \mathbf{F} we can consider the most common situation where a laminar electrode array with equidistant electrode contacts is inserted perpendicularly into, say, sensory cortex [13, 14, 54, 76, 79, 87]. For simplicity we further assume the stimulus-evoked CSD to be located in infinitely thin, circular disks centered on the N electrode contacts. Each disk is further assumed to have the same CSD throughout the disk and to be positioned in the horizontal plane perpendicular to an inserted laminar electrode array [66]. For this 'δ-source' method a simple

1.6. ESTIMATION OF CURRENT-SOURCE DENSITY (CSD) FROM LFP35

formula is obtained for the matrix elements, and the method also has some additional interest since it turns out to correspond to the standard CSD method in the limit of infinitely large discs [66]. From electrostatic theory we have that the extracellular potential at a position z at the center axis due to an infinitely thin current-source disk placed in z' is given by $\phi = (\sqrt{(z - z')^2 + R^2} - |z - z'|)C^p/2\sigma$, where C^p now is the *planar* CSD, R is the radius of the disks, and σ is the extracellular conductivity [62, 66]. This implies that the matrix elements f_{jk} of the matrix \mathbf{F} is given by

$$f_{jk} = \left(\sqrt{(z_j - z_k)^2 + R^2} - |z_j - z_k| \right) h/2\sigma , \quad (1.23)$$

where $C_j = C_j^p/h$ and $z_j - z_k = h(j - k)$. This δ -source iCSD method is now completely specified by Eqs. (1.22) and (1.23), and as shown, e.g., in Fig. 7 of Ref. [66], even this simple δ -source CSD method completely outperforms the standard CSD method when the population activity is spatially confined.

In Ref. [66] two other variations of the iCSD method were also investigated: the *step* iCSD method, where the CSD is assumed to be step-wise constant in the z -direction, and the *spline* iCSD method based on cubic-splines interpolation. A GUI-based MATLAB toolbox for estimating the CSD from laminar multielectrode recordings has been developed based on these three iCSD methods and can be downloaded from <http://software.incf.org/>.

These two latter methods were generalized and further developed by Leski et al. [38] who developed iCSD method for estimation of CSD based on three-dimensional recordings. In this situation the advantage of the iCSD method is even larger compared to the standard CSD method in that the fraction of electrode contacts at the boundary is much higher. For example, their electrode grid consisted of $4 \times 5 \times 7$ contacts, for which 110 of the 140 electrode contacts are the boundary and thus outside the scope of the standard CSD method. From their studies Leski et al. concluded that a spline iCSD method was a good choice for this three-dimensional situation [38].

The iCSD method has now also been implemented for the case with two-dimensional recordings [39], e.g., recordings done with multishank laminar electrodes [9]. As for the 1D method, a GUI-based MATLAB toolbox has been developed to facilitate easy use of the method [39] and can be downloaded from <http://software.incf.org/>.

1.6.3 Validation of iCSD with population forward modeling

The results from forward-modeling of synaptically evoked activity in a population of morphologically reconstructed pyramidal neurons in Section 1.5 are well suited to test the iCSD approach, and to compare the accuracy of this method with the standard CSD method. Here we consider the situation where the LFP is recorded by a laminar electrode array oriented

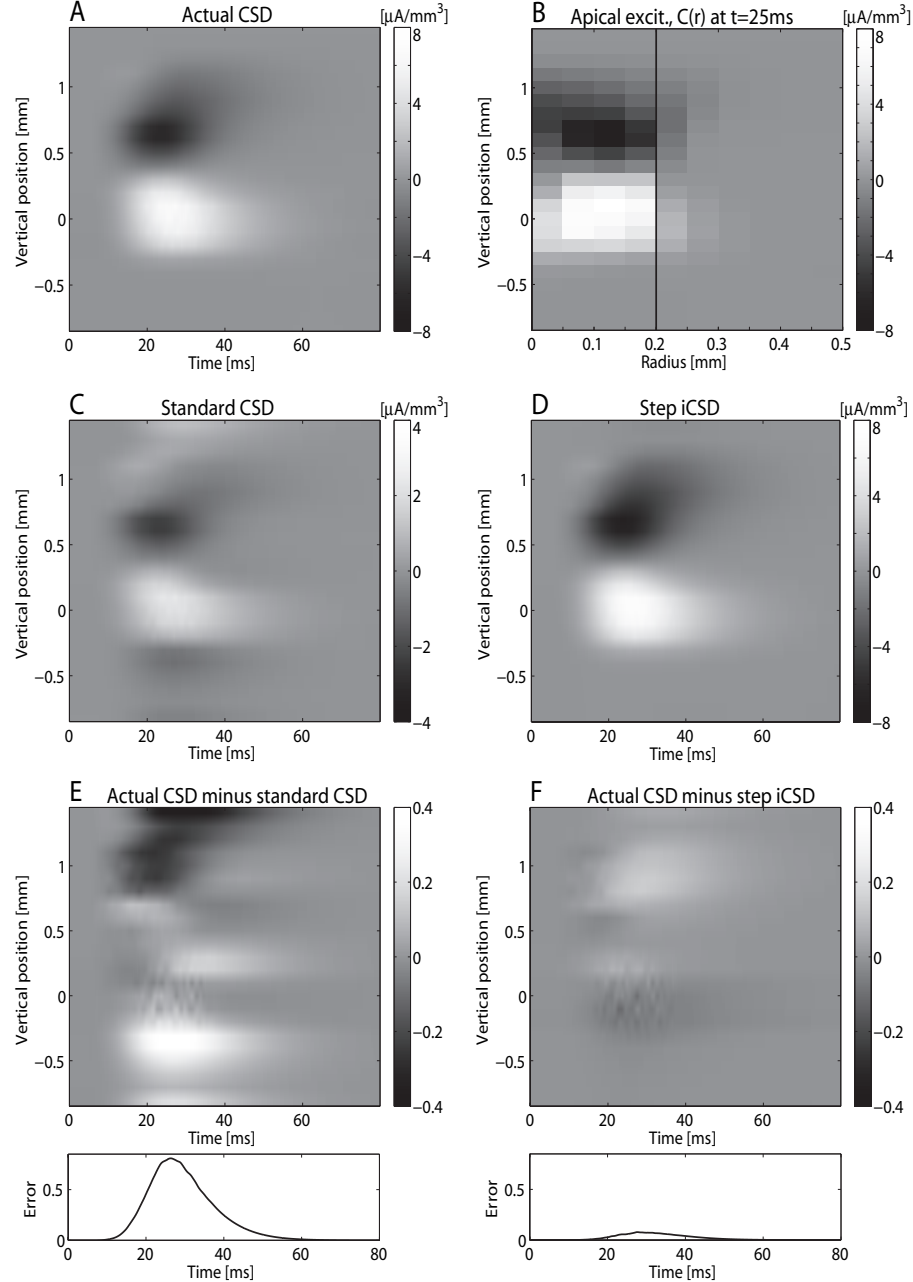


Figure 1.11: Illustration of CSD of model population and CSD estimation errors for different CSD methods. (A) Actual CSD within the column, i.e., average of CSD in centered cylindrical volume of height 0.1 mm and diameter 0.4 mm. (B) Radial CSD distribution at particular point in time ($t = 25$ ms) as a function of depth and radial distance from population center. Computed by averaging over volume elements consisting of annuli with rectangular cross-sectional area of $0.05 \text{ mm} \times 0.1 \text{ mm}$. (C) CSD estimate from using the standard CSD-method on the modelled LFPs along center axis of the population. Top and bottom estimates are found by the using the method of Ref. [88]. (D) CSD estimate from the step iCSD method. (E-F) Difference between the actual CSD and estimates from the standard (E) and step iCSD methods (F), respectively. Both the actual CSD and the estimated CSDs were normalized to have a maximum amplitude of unity prior to error estimation and plotting [68].

1.6. ESTIMATION OF CURRENT-SOURCE DENSITY (CSD) FROM LFP37

perpendicular to the cortical layers and penetrating the population through its center [68], but these forward-modeling population results have also been used for testing of the iCSD approach for recordings with multishank laminar electrodes [39].

As discussed above the CSD should be considered as the average net transmembrane current within a particular volume element. In Fig. 1.11A we show the actual CSD at the center of the columnar model population shown in Fig. 1.8, i.e., the average transmembrane current of a centered cylindrical volume element of height 0.1 mm and radius 0.2 mm, plotted as a function of time. The spatial spread of this CSD is illustrated in Fig. 1.11B. Here, the CSD at a particular time ($t = 25$ ms, cf. Fig. 1.9A) was computed for cylindrical annuli with rectangular cross-sectional areas of $0.05 \text{ mm} \times 0.1 \text{ mm}$. It is seen that the CSD varies only moderately as a function of radial distance when inside the column. One further sees that even though the somas are restricted to radial distances less than 0.2 mm, the dendrites gives non-negligible CSD outside this boundary.

The next four panels in Fig. 1.11 illustrate the accuracy of the CSD estimation methods in this model situation. The estimated CSD along the (virtual) laminar electrode from the standard CSD method is shown in Fig. 1.11C. This CSD is estimated by using Eq. (1.20) on model LFPs at the (virtual) electrode contacts at the center axis of the column, cf. Fig. 1.8B, except at the top and bottom contacts where the method of Ref. [88] is used. Comparison with Fig. 1.11A shows that the standard CSD method predicts spurious sinks and sources below and above the actual CSD. Further, the size (amplitude) of the actual sources and sinks are underestimated by about a factor of two.

Fig. 1.11D shows the CSD estimated from the step iCSD method [68]. This method assumes piecewise constant CSD distribution in the vertical direction. A columnar diameter of 0.4 mm is assumed in the iCSD method, the diameter of the cylindrical box to which the soma positions are restricted. This is clearly less than the spatial extension of the actual CSD seen in Fig. 1.11B, but anyhow a natural parameter choice. Despite the somewhat unnatural assumptions regarding the form of the CSD, the step iCSD estimates are seen to be very similar to the actual CSD seen in Fig. 1.11A. The much improved CSD estimates from the step iCSD method compared to the standard CSD method is further illustrated in the panels E and F showing the relative mean-square differences between the actual and estimated CSD for the two CSD estimation methods (see Ref. [68] for detailed specification of the error estimate); the error of the standard CSD method estimates is much larger than for the iCSD step method. For further discussion see Pettersen et al. [68].

1.7 Concluding remarks

The main topic of this chapter has been the forward-modeling of extracellular potentials, i.e., the calculation the extracellular potentials from activity in neurons or populations of neurons. So far there has been relatively few modeling studies pursuing such calculations; in fact, the first full-fledged study of this type using morphologically reconstructed neurons was done less than fifteen years ago [30]. With the advent of new public databases of reconstructed neurons such as <http://www.neuromorpho.org/> and ever more powerful computers, we expect that the relatively straightforward forward-modeling scheme for calculating extracellular potentials will be more frequently used in the years to come.

An important set of applications of this forward-modeling scheme will be the validation of methods for analysis of LFP and MUA data, as exemplified by the testing of the iCSD method in Fig. 1.11 or the testing of the MUA as a measure of population firing rate, cf. Fig. 1.9D and Ref. [68]. The forward-modeling scheme will likewise be useful for testing and development of new methods for analysis of multielectrode data such as the so called *laminar population analysis (LPA)* [14] or spike-sorting algorithms [9, 41].

To improve the accuracy and reliability of the forward-modeling scheme it is important to establish good, experimentally validated models for the impedance properties of the extracellular media in all relevant types of neural tissue. Ideally one could envision experimental setups and protocols allowing for *in situ* measurement of the extracellular conductivity in conjunction with each multielectrode recording. Further, a more detailed understanding and accurate model representation of the electrical properties of the various types of multielectrodes are needed [25, 55, 59, 60].

Acknowledgement

Trygve Solstad and Øystein Sørensen are acknowledged for a thorough reading of the chapter. This work was supported by the Research Council of Norway (eVita, NOTUR, NevroNor).

Bibliography

- [1] Bédard, C., Kröger, H., and Destexhe, A. (2004). Modeling extracellular field potentials and the frequency-filtering properties of extracellular space. *Biophys J* **86**, 1829–1842.
- [2] Bédard, C., Kröger, H., and Destexhe, A. (2006a). Does the 1/f frequency scaling of brain signals reflect self-organized critical states? *Phys Rev Lett* **97**, 118102.
- [3] Bédard, C., Kröger, H., and Destexhe, A. (2006b). Model of low-pass filtering of local field potentials in brain tissue. *Phys Rev E Stat Nonlin Soft Matter Phys* **73**, 051911.
- [4] Bédard, C. and Destexhe, A. (2009). Macroscopic models of local field potentials and the apparent 1/f noise in brain activity. *Biophys J* **96**, 2589–2603.
- [5] Berens, P., Keliris, G.A., Ecker, A.S., Logothetis, N., and Tolias, A.S. (2008) Comparing the feature selectivity of the gamma-band of the local field potential and the underlying spiking activity in primate visual cortex. *Frontiers in Systems Neuroscience*, 10.3389/neuro.06/002.2008
- [6] Blomquist, P., Devor, A., Indahl, U. G., Ulbert, I., Einevoll, G. T., and Dale, A. M. (2008) Estimation of thalamocortical and intracortical network models from joint thalamic single-electrode and cortical laminar-electrode recordings in the rat barrel system, *submitted*.
- [7] Bower, J. M. and Beeman, D. (1998). *The Book of GENESIS: Exploring Realistic Neural Models with the GEneral NEural SImulation System, Second edition* (Springer-Verlag, New York).
- [8] Buzsaki, G. (2006). *Rhythms of the brain* (Oxford University Press, New York, NY).
- [9] Buzsáki, G. (2004). Large-scale recording of neuronal ensembles. *Nat Neurosci* **7**, 446–451.
- [10] Carnevale, N. T. and Hines, M. L. (2006). *The NEURON Book* (Cambridge University Press).
- [11] Csicsvari, J., Hirase, H., Czurkó, A., Mamiya, A., and Buzsáki, G. (1999). Oscillatory coupling of hippocampal pyramidal cells and interneurons in the behaving Rat. *J Neurosci* **19**, 274–287.

- [12] Dayan, P. and Abbott, L. F. (2001). *Theoretical Neuroscience* (MIT Press).
- [13] Di, S., Baumgartner, C., and Barth, D. S. (1990). Laminar analysis of extracellular field potentials in rat vibrissa/barrel cortex. *J Neurophysiol* **63**, 832–840.
- [14] Einevoll, G. T., Pettersen, K. H., Devor, A., Ulbert, I., Halgren, E., and Dale, A. M. (2007). Laminar population analysis: estimating firing rates and evoked synaptic activity from multielectrode recordings in rat barrel cortex. *J Neurophysiol* **97**, 2174–2190.
- [15] Fee, M. S., Mitra, P. M., Kleinfeld, D. (1996). Automatic sorting of multiple unit neuronal signals in the presence of anisotropic and non-Gaussian variability *J Neurosci Methods* **69**, 175–188.
- [16] Franke, F., Natora, M., Boucsein, C., Munk, M. H. J., and Obermayer K. (2010). An online spike detection and spike classification algorithm capable of instantaneous resolution of overlapping spikes. *J Comp Neurosci*
- [17] Freeman, J. A. and Nicholson, C. (1975). Experimental optimization of current source-density technique for anuran cerebellum. *J Neurophysiol* **38**, 369–382.
- [18] Freeman, W. J., Holmes, M. D., Burke, B.C., and Vanhalo, S. (2003) Spatial spectra of scalp EEG and EMB from awake humans. *Clinical Neurophysiology* **114**, 1053–1068.
- [19] Freeman, W. J. and Zhai, J. (2009) Simulated power spectral density (PSD) of background electrocorticogram (ECoG). *Cogn Neurodyn* **3**, 97–103.
- [20] Gabriel, S., Lau, R. W., and Gabriel, C. (1996). The dielectric properties of biological tissues: III. Parametric models for the dielectric spectrum of tissues. *Phys Med Biol* **41**, 2271–2293.
- [21] Gold, C., Henze, D. A., and Koch, C. (2007). Using extracellular action potential recordings to constrain compartmental models. *J Comput Neurosci* **23**, 39–58.
- [22] Gold, C., Henze, D. A., Koch, C., and Buzsáki, G. (2006). On the origin of the extracellular action potential waveform: A modeling study. *J Neurophysiol* **95**, 3113–3128.
- [23] Goto, T., Hatanaka, R., Ogawa, T., Sumiyoshi A., Riera, J., and Kawashima, R. (2010) An evaluation of the conductivity profile in the somatosensory barrel cortex of Wistar rats. *J Neurophysiol* **104**, 3388–3412.
- [24] Gray, C. M., Maldonado, P. E., Wilson, M., and McNaughton, B. (1995). Tetrodes markedly improve the reliability and yield of multiple single-unit isolation from multi-unit recordings in cat striate cortex. *J Neurosci Methods* **63**, 43–54.
- [25] Grimnes, S. and Martinsen, Ø. G. (2008). *Bioimpedance and Bioelectricity basics*, 2nd ed. (Academic Press).

- [26] Hämäläinen, M., Hari, R., Ilmoniemi, R., Knuutila, J., and Lounasmaa, O. (1993). Magnetoencephalography theory, instrumentation, and applications to noninvasive studies of the working human brain. *Rev Mod Phys* **65**, 413–497.
- [27] Harris, K. D., Henze, D. A., Csicsvari, J., Hirase, H., and Buzsaki, G. (2000) Accuracy of tetrode spike separation as determined by simultaneous intracellular and extracellular measurements. *J Neurophysiol* **84**, 401–414.
- [28] He, B. J., Zempel, J. M., Snyder, A. Z., Raichle, M. E. (2010) The temporal structures and functional significance of scale-free brain activity. *Neuron* **66**, 353–369.
- [29] Henze, D. A., Borhegyi, Z., Csicsvari, J., Mamiya, A., Harris, K. D., and Buzsaki, G. (2000) Intracellular features predicted by extracellular recordings in the hippocampus in vivo. *J Neurophysiol* **84**, 390–400.
- [30] Holt, G. R. and Koch, C. (1999). Electrical interactions via the extracellular potential near cell bodies. *J Comput Neurosci* **6**, 169–184.
- [31] Hubel, D. H. (1957). Tungsten Microelectrode for Recording from Single Units. *Science* **125**, 549–550.
- [32] Jackson, J. (1998). *Classical electrodynamics* (Wiley, Hoboken, NJ).
- [33] Jog, M. S., Connolly, C. I., Kubota, Y., Iyengar, D. R., Garrido, L., Harlan, R., and Graybiel, A. M. (2002). Tetrode technology: advances in implantable hardware, neuroimaging, and data analysis techniques. *J Neurosci Methods* **117**, 141–152.
- [34] Johnston, D. and Wu, S. M.-S. (1994). *Foundation of Cellular Neurophysiology* (MIT Press).
- [35] Katzner, S., Nauhaus, I., Benucci, A., Bonin, V., Ringach, D. L., and Carandini, M. (2009). Local origin of field potentials in visual cortex. *Neuron* **61**, 35–41.
- [36] Kim, S. and McNames, J. (2007). Automatic spike detection based on adaptive templatage matching for extracellular neural recordings. *J Neurosci Meth* **165**, 165–174.
- [37] Kreiman, G., Hung, C.P, Kraskov, A., Quiroga, R.Q., Poggio, T., and DiCarlo, J.J. (2006) Object selectivity of local field potentials and spikes in the macaque inferior temporal cortex. *Neuron* **49**, 433–445.
- [38] Leski, S., Wojcik, D. K., Tereszczuk, J., Swiejkowski, D. A., Kublik, E., and Wrobel, A. (2007). Inverse current-source density method in 3D: reconstruction fidelity, boundary effects, and influence of distant sources. *Neuroinformatics* **5**, 207–222.
- [39] Leski, S., Pettersen, K. H., Tunstall, B., Einevoll, G. T., Gigg, J., and Wojcik, D. K. (2011). Inverse Current Source Density method in two dimensions: Inferring neural activation from multielectrode recordings. *Neuroinformatics, in press*

- [40] Levina, A., Herrmann, J. M., and Geisel, T. (2007) Dynamical synapses causing self-organized criticality in neural networks. *Nature Physics* **3**, 857–860.
- [41] Lewicki, M. S. (1998). A review of methods for spike sorting: the detection and classification on neural action potentials. *Network: Comp. Neural Syst.* **9**, R53–R78.
- [42] Lindén, H., Pettersen, K. H., Tetzlaff, T., Potjans, T., Denker, M., Diesmann, M., Grün, S., Einevoll, G. T. (2009). Estimating the spatial range of local field potentials in a cortical population model. *BMC Neurosci* **10**(Suppl. 1), 224.
- [43] Lindén, H., Potjans, T., Einevoll, G. T., Denker, M., Grün, S., and Diesmann, M. (2009). Modeling the large-scale layered cortical network model. *Frontiers in Neuroinformatics*. Conference Abstract: 2nd INCF Congress of Neuroinformatics. doi: 10.3389/conf.neuro.11.2009.08.046
- [44] Lindén, H., Pettersen K. H., and Einevoll, G. T. (2010) Intrinsic dendritic filtering gives low-pass power spectra of local field potentials. *J Comput Neurosci* **29**, 423–444
- [45] Linkenkaer-Hansen, K., Nikouline, V. V., Palva, J. M., and Ilmoniemi, R. J. (2001). Long-Range Temporal Correlations and Scaling Behavior in Human Brain Oscillations *J Neurosci* **21**, 1370–1377
- [46] Liu, J. and Newsome, W. T. (2006) Local field potential in cortical area MT. Stimulus tuning and behavioral correlations, *J Neurosci* **26**, 7779–7790.
- [47] Logothetis, N. K., Kayser, C., and Oeltermann, A. (2007). In vivo measurement of cortical impedance spectrum in monkeys: implications for signal propagation. *Neuron* **55**, 809–823.
- [48] López-Aguado, L., Ibarz, J. M., and Herreras, O. (2001) Acitivity-dependent changes of tissue resistivity in the CA1 region in vivo are layer-specific: Modulation of evoked potentials. *Neuron* **108**, 249–262.
- [49] Mainen, Z. F. and Sejnowski, T. J. (1996). Influence of dendritic structure on firing pattern in model neocortical neurons. *Nature* **382**, 363–366.
- [50] McNaughton, B. L., O’Keefe, J., and Barnes, C. A. (1983). The stereotrode: a new technique for simultaneous isolation of several single units in the central nervous system from multiple unit records. *J Neurosci Methods* **8**, 391–397.
- [51] Miller, K. J., Sorensen, L. B., Ojemann, J. G., and den Nijs, M. (2009). Power-law scaling in the brain surface electric potential. *PLoS Comp Biol* **5**, e1000609.
- [52] Milstein, J. N. and Koch, C. (2008). Dynamic moment analysis of the extracellular electric field of a biologically realistic spiking neuron. *Neural Comput* **20**, 2070–2084.
- [53] Milstein, J., Mormann, F., Fried, I., and Koch., C (2009). Neuronal shot noise and Brownian $1/f^2$ behavior in the local field potential. *PLoS ONE* **4**, e4338.

- [54] Mitzdorf, U. (1985). Current source-density method and application in cat cerebral cortex: investigation of evoked potentials and EEG phenomena. *Physiol Rev* **65**, 37–100.
- [55] Moffitt, M. A. and McIntyre C. C. (2005). Model-based analysis of cortical recording with silicon microelectrodes. *Clin Neurophysiol* **116**, 2240–2250.
- [56] Monto, S., Palva, S., Voipio J., and Palva, J. M. (2008) Very slow EEG fluctuations predict the dynamics of stimulus detection and oscillation amplitudes in humans. *J Neurosci* **28**, 8268–8272.
- [57] Mountcastle, V. B. (1997). The columnar organization of the neocortex. *Brain* **120**, 701–722.
- [58] Nadasdy, Z., Csicsvari, J., Penttonen, M., Hetke, J., Wise, K., and Buzsaki, G. (1998). Extracellular recording and analysis of neuronal activity: From single cells to ensembles, in *Neuronal Ensembles*, ed. H. Eichenbaum and J. L. Davis (Wiley: New York).
- [59] Nelson, M. J., Pouget, P., Nilsen, E. A., Patten, C. D., and Schall, J. D. (2008) Review of signal distortion through metal microelectrode recording circuits and filters. *J Neurosci Methods* **169**, 141–157.
- [60] Nelson, M. J. and Pouget, P. (2010) Do electrode properties create a problem in interpreting local field potential recordings? *J Neurophysiol* **103**, 2325–2317.
- [61] Nicholson, C. and Freeman, J. A. (1975). Theory of current source-density analysis and determination of conductivity tensor for anuran cerebellum. *J Neurophysiol* **38**, 356–368.
- [62] Nicholson, C. and Llinas, R. (1971). Field potentials in the alligator cerebellum and theory of their relationship to Purkinje cell dendritic spikes. *J Neurophysiol* **34**, 509–531.
- [63] Nicholson, C. and Llinás, R. (1975). Real time current source-density analysis using multi-electrode array in cat cerebellum. *Brain Res* **100**, 418–424.
- [64] Normann, R. A., Maynard, E. M., Rousche, P. J., and Warren, D. J. (1999). A neural interface for a cortical vision prosthesis. *Vision Res* **39**, 2577–2587.
- [65] Nunez, P. L. (2006). *Electric Fields of the Brain: The Neurophysics of EEG* (Oxford University Press).
- [66] Pettersen, K. H., Devor, A., Ulbert, I., Dale, A. M., and Einevoll, G. T. (2006). Current-source density estimation based on inversion of electrostatic forward solution: Effects of finite extent of neuronal activity and conductivity discontinuities. *J Neurosci Methods* **154**, 116–133.
- [67] Pettersen, K. H. and Einevoll, G. T. (2008). Amplitude variability and extracellular low-pass filtering of neuronal spikes. *Biophys J* **94**, 784–802.
- [68] Pettersen, K. H., Hagen, E., and Einevoll, G. T. (2008). Estimation of population firing rates and current source densities from laminar electrode recordings. *J Comput Neurosci* **24**, 291–313.

- [69] Pettersen, K.H. and Einevoll, G.T. (2009). Neurophysics: what the telegrapher's equation has taught us about the brain, in *An anthology of developments in clinical engineering and bioimpedance: Festschrift for Sverre Grimnes*, Ø. Martinsen and Ø. JENSEN (eds.) (Unipub, Oslo).
- [70] Pouzat C. and Chaffiol, A. (2009). Automatic spike train analysis and report generation. An imnplementation with R, R2HTML and STAR. *J Neurosci Meth* **181**, 119–144.
- [71] Pritchard, W.S. (1992). The brain in fractal time: 1/f-like power spectrum scaling of the human electroencephalogram. *International J Neurosci* **66**, 119–129.
- [72] Quian Quiroga, R., Nadasdy, R., and Ben-Shaul, Y. (2004). Unsupervised spike detection and sorting with wavelets and superparamagnetic clustering. *Neural Comp* **16**, 1661–1687.
- [73] Quian Quiroga, R. (2007). Spike sorting. *Scholarpedia* **2**, 3583.
- [74] Rall, W. (1962). Electrophysiology of a dendritic neuron model. *Biophys J* **2**, 145–167.
- [75] Rall, W. and Shepherd, G. M. (1968). Theoretical reconstruction of field potentials and dendrodendritic synaptic interactions in olfactory bulb. *J Neurophysiol* **31**, 884–915.
- [76] Rappelsberger, P., Pockberger, H., and Petsche, H. (1981). Current source density analysis: methods and application to simultaneously recorded field potentials of the rabbit's visual cortex. *Pflügers Arch* **389**, 159–170.
- [77] Recce, M. and O'Keefe, J. (1989). The tetrode: a new technique for multi-unit extracellular recording. In *Soc. Neurosci. Abstr.* **15**:1250.
- [78] Rutishauser, U., Schuman, E. M., Mamelak, A. N., Online detection and sorting of extracellularly recorded action potentials in human medial temporal lobe recordings in vivo. *J Neurosci Methods* **154**, 204–224.
- [79] Schroeder, C. E., Lindsley, R. W., Specht, C., Marcovici, A., Smiley, J. F., and Javitt, D. C. (2001). Somatosensory input to auditory association cortex in the macaque monkey. *J Neurophysiol* **85**, 1322–1327.
- [80] Segev, I. and Burke, R. (1998). Compartmental model of complex neurons, in *Methods in Neuronal Modeling: From Ions To Network*, ed. C. Koch and I. Segev (MIT Press, Cambridge, MA).
- [81] Shoham, S. and Nagarajan, S. S. (2004) . The theory of CNS recording, in *Neuroprosthetics: Theory and Applications*, ed. K. W. Horch and G. S. Dhillon, pp. 448–471 (World Scientific, New Jersey)
- [82] Shoham, S., O'Connor, D. H., and Segev, R. (2006). How silent is the brain: is there a "dark matter" problem in neuroscience? *J Comp Physiol A* **192**, 777–784.
- [83] Smith, L.S. and Mtetwa, N. (2007). A tool for synthesizing spike trains with realistic interference. *J Neurosci Methods* **159**, 170–180.

- [84] Stuart, G., Spruston, N., and Häusser, M. (eds.) (2007). *Dendrites*, 2nd ed. (Oxford University Press, Oxford).
- [85] Sukov, W. and Barth, D. S. (1998). Three-dimensional analysis of spontaneous and thalamically evoked gamma oscillations in auditory cortex. *J Neurophysiol* **79**, 2875–2884.
- [86] Takekawa, T., Isomura, Y., and Fukai, T. (2010) Accurate spike sorting for multiunit recordings. *European J Neurosci* **31**, 263–272.
- [87] Ulbert, I., Halgren, E., Heit, G., and Karmos, G. (2001). Multiple microelectrode-recording system for human intracortical applications. *J Neurosci Methods* **106**, 69–79.
- [88] Vaknin, G., DiScenna, P. G., and Teyler, T. J. (1988). A method for calculating current source density (CSD) analysis without resorting to recording sites outside the sampling volume. *J Neurosci Methods* **24**, 131–135.
- [89] Wehr, M., Pezaris, J. S., and Sahani, M. (1999) Simultaneous paired intracellular and tetrode recordings for evaluation the performance of spike sorting algorithms. *Neurocomp* **26-27**, 1061–1068.
- [90] Wilson, M. A. and McNaughton, B. L. (1993). Dynamics of the hippocampal ensemble code for space. *Science* **261**, 1055–1058.
- [91] Xing, D., Yeh, C.-I., and Shapley, R. M. (2009) Spatial spread of the local field potential and its laminar variation in visual cortex. *J Neurosci* **29**, 11540–11549.